Advances in Nano Research, *Vol. 17, No.4 (2024) 385-399*
https://doi.org/10.12989/anr.2024.17.4.385

Application of artificial intelligence to improve the efficiency and stability of prosthetic hands via nanoparticle reinforcement

Jialing Li[1], Gongxing Yan*[2], Zhongjian Tang[1], Saifeldin M. Siddeeg[3] and Tamim Alkhalifah[4]

[1]*School of Artificial intellegence, Chongqing Youth Vocational & Technical College; Chongqing 401320, China*
[2]*Luzhou vocational and technical college, Luzhou 646000, Sichuan, China*
[3]*Department of Chemistry, College of Science, King Khalid University, P.O. Box 9004, 61413 Abha, Saudi Arabia*
[4]*Department of Computer Engineering, College of Computer, Qassim University, Buraydah, Saudi Arabia*

(*Received September 10, 2021, Revised October 12, 2024, Accepted October 14, 2024*)

Abstract. NEMS (Nano-Electro-Mechanical Systems) devices play a significant role in the advancement of prosthetic hands due to their unique properties at the nanoscale. Their integration enhances the functionality, sensitivity, and performance of prosthetic limbs. Understanding the electro-thermal buckling behavior of such structures is crucial since they may be subjected to extreme heat. So, in this paper, the two-dimensional hyperbolic differential quadrature method (2D-HDQM) integrated with a four-variable refined quasi-3D tangential shear deformation theory (RQ-3DTSDT) in view of the trace of thickness stretching is extended to study electro-thermal buckling response of three-directional poroelastic FG (3D-PFG) circular sector nanoplate patched with piezoelectric layer. Aimed at discovering the real governing equations, coupled equations with the aid of compatibility conditions are employed. Regarding modeling the size-impacts, nonlocal refined logarithmic strain gradient theory (NRLSGT) with two variables called nonlocal and length scale factors is examined. Numerical experimentation and comparison are used to indicate the precision and proficiency related to the created procedure. After obtaining the outputs of the mathematics, an appropriate dataset is used for testing, training and validating of the artificial intelligence. In the results section will be discussed the trace associated with multiple geometrical and physical factors on the electro-thermal buckling performance of the current nanostructure. These findings are essential for the design and optimization of NEMS applications in various fields, including sensing, actuation, and electronics, where thermal stability is paramount. The study's insights contribute to the development of more reliable and efficient NEMS devices, ensuring their robust performance under varying thermal conditions.

Keywords: artificial intelligence; circular NEMS; electro-thermal buckling; prosthetic hands; 2D-HDQM

1. Introduction

Due to its unique capacity to integrate mechanical and electrical characteristics, piezoelectric materials are applied with actuators and sensors to control and monitor the system's response (Drai *et al.* 2023, Esen *et al.* 2023, Zhang *et al.* 2023, 2024, Eghbali and Hosseini 2024, Ghazwani *et al.* 2024). Minco has supplied temperature sensors for aerospace applications for over 50 years. During this long history, the ultra-high reliability needs of the aerospace market have become engrained in our methods and processes. As with most good stories, it starts at the beginning – with our New Product Introduction (NPI) process. Our team-based approach is a phased multi-step program highlighted by customer requirement analysis, risk assessments and design for manufacturability (DFM) reviews at the bid stage, followed by a comprehensive design and process risk analysis, leading to prototyping and post-build reviews targeted at confirming or further refining the design and processes. One of the application of the temperature sensor for aerospace industries can be shown in Fig. 1.

Functionally Graded Piezoelectric Material (FGPM), a specific type of piezoelectric material, is a novel type of FGM whose structure and properties are routinely changing in the required directions. It was created specifically to possess desired qualities for a certain use. Smart structures or components fabricated from FGPM are superior to conventional sensors and actuators, which are typically fabricated from uni, bi, and multi morphic type of materials. Numerous investigate projects similarly examine the conduct of the FGPM. Studies on the static and dynamic performances related to the FGPM structure, counting plates and beams, have recently been published (Kumar and Harsha 2020). In addition, shells, plates, and beams, among others, are frequently used in many different kinds of manufacturing. Circular sector plate structures are exclusive engineering structures used in many different subdivisions. The varied behaviors of these structures have been investigated by testing numerous enhancements and conditions, such as multiple materials, multiple loadings, Boundary Conditions (BCs), and many other situations. Nowadays Many scientists have been interested in this topic as a result of the numerous and cutting-edge applications of piezoelectric materials and structures. A modal analysis on a rectangular plate composed of FGPM was undergone by Kumar and Harsha (Kumar and Harsha 2020). A method for analogue modeling related to piezoelectric beams was

---

*Corresponding author, Ph.D.,
E-mail: yaaangx@126.com

ISSN: 2287-237X (Print), 2287-2388 (Online)

Fig. 1. One of the applications of the NEMS device for prosthetic hands

presented by Chen *et al*. (2019). Silva *et al*. developed analogous electrical circuits regarding linear and nonlinear electromechanically linked systems (Silva *et al*. 2018). Zhou and Luo used the effects of various external loadings to determine how multilayer piezoelectric devices reacted to asymmetric non-slipping adhesion (Zhou and Luo 2022). The Electromechanical performance of nonlinear piezo-electric structures was examined by Wu *et al*. (Wu *et al*. 2022). With consideration for the nanoscale size impact according to the nonlocal scheme, the propagation related to the Bleustein-Gulyaev wave in a nonlocal piezoelectric layer was investigated by Sharma and Kumar (Sharma and Kumar 2022). The effect associated with the initial stress on the parameters related to wave propagation regrding the piezoelectric layer system was examined by Jin *et al*. (Jin *et al*. 2005). The electromechanical performance related to shell structures integrated piezoelectric layers was predicted by Mallek *et al*. employing a 3D-shell form according to a discrete double directors shell element (Mallek *et al*. 2019). Mallek *et al*. investigated the non-linear performance related to the smart piezoelectric structures in respect to volume percentage, nanotube distribution, geometrical characteristics, and load boundary (Mallek *et al*. 2019). Moradi-Dastjerdi *et al*. demonstrated the resistance to buckling of a innovative active multifunctional sandwich plate under a temperature change (Moradi-Dastjerdi *et al*. 2020). The free vibration performance related to a multi-functional smart sandwich plate implementing a cutting-edge and consistent technology were examined by Moradi-Dastjerdi and Behdinan (Moradi-Dastjerdi and Behdinan 2021). Khaje khabaz *et al*. obtained active vibration for a micro-beam combined with piezoelectric sensor and actuator according to modified couple stress and surface stress elasticity theories (Khaje khabaz *et al*. 2020). Selim *et al*. determined the active vibration management related to functionally graded multilayer composite plates (Selim *et al*. 2019). Thermal buckling investigation associated with a multilayer, FGPM beam exposed to external electric voltage and humid situations was demonstrated by Sobhy *et al*. (2022). A novel deformation approach was implemented to evaluate the nonlinear vibration examination related to nanobeams exposed to magneto-electro-thermal loading by Xiao *et al*. (2022). Kumar and Harsha examined a hybrid ceramic-metal plate whose features fluctuate in accordance with Power-law and Sigmoid law distributions under thermo-electro-mechanical stress regarding its static, buckling, and vibration performances (Kumar and Harsha 2022). Alazwari *et al*. studied the buckling performance related to the graphene-based piezoelectric circular nanoplates that were placed atop elastic media and under an outward electric domain (Alazwari *et al*. 2022). The relationship between temperature, external electric actuation, and axial mechanical load on FGPM cylindrical micropanels' microstructural features of nonlinear stability were investigated by Alshenawy *et al*. (2022).

Modeling is a critical tool for engineers, serving as a bridge between theoretical concepts and practical applications (Wang *et al*. 2023, Li *et al*. 2024). It allows engineers to simulate real-world scenarios, making it possible to analyze complex systems without the need for physical prototypes (Cao *et al*. 2024, Zhang *et al*. 2024). By creating mathematical or computational representations of engineering problems, models enable the exploration of different design options and operational strategies (Huang *et al*. 2021, Du *et al*. 2024). This predictive capability is essential in optimizing performance, enhancing safety, and reducing costs (Huang *et al*. 2022a, b). Moreover, modeling helps engineers understand the behavior of systems under various conditions, including extreme scenarios that are difficult to test experimentally (Huang *et al*. 2023, Zhang and Zhang 2023). It facilitates the identification of potential issues early in the design process, allowing for timely modifications and improvements (Liu *et al*. 2020, Yang *et al*. 2023). The iterative nature of modeling also supports innovation, enabling engineers to refine their ideas through simulation and analysis (Yang *et al*. 2022, 2023). In fields like structural engineering, modeling is crucial for assessing the integrity and stability of structures before construction (Chen *et al*. 2023, Song *et al*. 2024). In fluid dynamics, it assists in predicting flow patterns and interactions, which are vital for designing efficient systems (Hu *et al*. 2023, Wu *et al*. 2023). Additionally, modeling plays a key role in environmental engineering, helping to evaluate the impact of projects on ecosystems and communities (Feng *et al*. 2021, Firouzianhaji *et al*. 2021). Furthermore, the integration of modeling with data analytics and machine learning enhances predictive accuracy, providing deeper insights into system behavior (Mehrabi *et al*. 2021). As engineering challenges become more complex, the importance of effective modeling continues to grow (Taheri *et al*. 2019). It not only aids in problem-solving but also supports informed decision-making throughout the engineering lifecycle. Ultimately, robust modeling practices are essential for delivering innovative, sustainable, and safe engineering solutions (Toghroli *et al*. 2020, Mehrabi *et al*. 2021).

The goal of Ref. (Qiu and Wang 2024) was to improve economic stability via more focused financial strategies and risk management by using sophisticated algorithms to classify credit card users based on their financial behavior. In order to effectively capture and evaluate tail risks in financial markets, extreme value theory in conjunction with mixture models is utilized in Ref. (Qiu 2019) to estimate the probability of uncommon but significant financial losses. NEMS-based sensors are used to detect thermal and mechanical stresses in aerospace structures. Knowledge of their thermal buckling properties ensures these sensors remain accurate and reliable under extreme thermal conditions, providing crucial data for structural health monitoring. Based on the literature survey, there have been no former investigations of electro-thermal buckling for 3D-PFG circular sector nanoplates patched with piezo-electric layer utilizing the RQ-3DLSDT-based 2D-HDQM and taking into account the temperature influence related to piezoelectric coefficients. The additional objective associated with current work is to evaluate the electro-thermal buckling examination related to a 3D-PFG circular sector nanoplate patched through a piezoelectric layer in a thermal environment that is more representative of the real-world condition. After obtaining the outputs of the mathematics, an appropriate dataset is used for testing, training and validating of the artificial intelligence. The remaining sections are ordered by. In Section 2, a mathematical form for a 3D-PFG circular sector nanoplate with a piezoelectric layer is derived. The technique of deriving 2D-HDQM for solving the motion equations for a 3D-PFG circular sector nanoplate patched with a piezo-electric layer is described in Section 3. In Section 4, artificial intelligence algorithm is used. In Section 5, the authors offer several numerical investigations to examine the correctness and efficacy related to the existing RQ-3DLSDT-based 2D-HDQM. We then investigate the temperature distribution and geometric response of a 3D-PFG circular sector nanoplate patched with a piezoelectric layer under thermo-electrical loads.

2. Material factors

2.1 Displacement domain

The part explains novel four-variable RQ-3DTSDT, which takes into account the impact of thickness stretching. The field of displacement is written out (Mantari and Soares 2015):

$$\begin{aligned}
\mathfrak{U}_c(\mathbb{r},\theta,\mathbb{z},t) &= \mathfrak{U}_{0c}(\mathbb{r},\theta,t)+\mathbb{z}\left(\alpha\frac{\partial\mathfrak{W}_{bc}(\mathbb{r},\theta,t)}{\partial\mathbb{r}}+\beta\frac{\partial\mathfrak{W}_{sc}(\mathbb{r},\theta,t)}{\partial\mathbb{r}}\right)+\mathcal{T}(\mathbb{z})\frac{\partial\mathfrak{W}_{sc}(\mathbb{r},\theta,t)}{\partial\mathbb{r}},\\
\mathfrak{V}_c(\mathbb{r},\theta,\mathbb{z},t) &= \mathfrak{V}_{0c}(\mathbb{r},\theta,t)+\mathbb{z}\left(\alpha\frac{\partial\mathfrak{W}_{bc}(\mathbb{r},\theta,t)}{\mathbb{r}\partial\theta}+\beta\frac{\partial\mathfrak{W}_{sc}(\mathbb{r},\theta,t)}{\mathbb{r}\partial\theta}\right)+\mathcal{T}(\mathbb{z})\frac{\partial\mathfrak{W}_{sc}(\mathbb{r},\theta,t)}{\mathbb{r}\partial\theta},\\
\mathfrak{W}_c(\mathbb{r},\theta,\mathbb{z},t) &= \mathfrak{W}_{bc}(\mathbb{r},\theta,t)+g(\mathbb{z})\mathfrak{W}_{sc}(\mathbb{r},\theta,t).
\end{aligned}\tag{1}$$

where $\mathcal{T}(\mathbb{z})=\frac{\mathrm{h}}{m}\tan\left(\frac{m\mathbb{z}}{h}\right)+\mathbb{z}^3$, $g(\mathbb{z})=\mathrm{n}\mathcal{T}'(\mathbb{z})$, $\alpha=y^{**}$, $\beta=q^{**}$, $y^{**}=-1$, $q^{**}=y^*+q^*$, $y^*=-\mathcal{T}'\left(\frac{h}{2}\right)$, and $q^*=-g\left(\frac{h}{2}\right)$ respectively. Also, the displacement domain regarding patch piezoelectric, are (Reddy 2003):

$$\begin{aligned}
\mathfrak{U}_p(\mathbb{r},\theta,\mathbb{z},t) &= -\mathbb{z}\frac{\partial\mathfrak{W}_{0p}(\mathbb{r},\theta,t)}{\partial\mathbb{r}},\\
\mathfrak{V}_p(\mathbb{r},\theta,\mathbb{z},t) &= -\mathbb{z}\frac{\partial\mathfrak{W}_{0p}(\mathbb{r},\theta,t)}{\mathbb{r}\partial\theta},\\
\mathfrak{W}_p(\mathbb{r},\theta,\mathbb{z},t) &= \mathfrak{W}_{0p}(\mathbb{r},\theta,t).
\end{aligned}\tag{2}$$

2.2 Compatibility conditions

Assuming ideal BCs by the side related to the top and bottom face layer-core edges, the compatibility connections can be given by:

$$\begin{aligned}
\mathfrak{U}_p\left(\mathbb{r},\theta,\frac{h_c}{2},t\right) &= \mathfrak{U}_c\left(\mathbb{r},\theta,\frac{h_c}{2},t\right),\\
\mathfrak{V}_p\left(\mathbb{r},\theta,\frac{h_c}{2},t\right) &= \mathfrak{V}_c\left(\mathbb{r},\theta,\frac{h_c}{2},t\right),\\
\mathfrak{W}_p\left(\mathbb{r},\theta,\frac{h_c}{2},t\right) &= \mathfrak{W}_c\left(\mathbb{r},\theta,\frac{h_c}{2},t\right),
\end{aligned}\tag{3}$$

And displacement domains may be reformulated using Eqs. (1)-(3) as follows:

$$\begin{aligned}
\mathfrak{U}_c(\mathbb{r},\theta,\mathbb{z},t) &= \mathfrak{U}_{0c}(\mathbb{r},\theta,t)+\mathbb{z}\left(\alpha\frac{\partial\mathfrak{W}_b(\mathbb{r},\theta,t)}{\partial\mathbb{r}}+\beta\frac{\partial\mathfrak{W}_s(\mathbb{r},\theta,t)}{\partial\mathbb{r}}\right)+\mathcal{T}(\mathbb{z})\frac{\partial\mathfrak{W}_s(\mathbb{r},\theta,t)}{\partial\mathbb{r}},\\
\mathfrak{V}_c(\mathbb{r},\theta,\mathbb{z},t) &= \mathfrak{V}_{0c}(\mathbb{r},\theta,t)+\mathbb{z}\left(\alpha\frac{\partial\mathfrak{W}_{bc}(\mathbb{r},\theta,t)}{\mathbb{r}\partial\theta}+\beta\frac{\partial\mathfrak{W}_{sc}(\mathbb{r},\theta,t)}{\mathbb{r}\partial\theta}\right)+\mathcal{T}(\mathbb{z})\frac{\partial\mathfrak{W}_{sc}(\mathbb{r},\theta,t)}{\mathbb{r}\partial\theta},\\
\mathfrak{W}_c(\mathbb{r},\theta,\mathbb{z},t) &= \mathfrak{W}_{bc}(\mathbb{r},\theta,t)+g(\mathbb{z})\mathfrak{W}_{sc}(\mathbb{r},\theta,t),\\
\mathfrak{U}_p(\mathbb{r},\theta,\mathbb{z},t) &= -\mathbb{z}\frac{\partial\mathfrak{W}_{bc}(\mathbb{r},\theta,t)}{\partial\mathbb{r}}-\mathbb{z}g\left(\frac{h_c}{2}\right)\frac{\partial\mathfrak{W}_{sc}(\mathbb{r},\theta,t)}{\partial\mathbb{r}},\\
\mathfrak{V}_p(\mathbb{r},\theta,\mathbb{z},t) &= -\mathbb{z}\frac{\partial\mathfrak{W}_{bc}(\mathbb{r},\theta,t)}{\mathbb{r}\partial\theta}-\mathbb{z}g\left(\frac{h_c}{2}\right)\frac{\partial\mathfrak{W}_{sc}(\mathbb{r},\theta,t)}{\mathbb{r}\partial\theta},\\
\mathfrak{W}_p(\mathbb{r},\theta,\mathbb{z},t) &= \mathfrak{W}_{bc}(\mathbb{r},\theta,t)+g(\mathbb{z})\mathfrak{W}_{sc}(\mathbb{r},\theta,t).
\end{aligned}\tag{4}$$

Herein, strain displacements are expressed by (Reddy 2003):

$$\begin{aligned}
&\mathcal{E}_{\mathbb{r}\mathbb{r}}=\frac{\partial\mathfrak{U}}{\partial\mathbb{r}},\mathcal{E}_{\theta\theta}=\frac{1}{\mathbb{r}}\left(\mathfrak{U}+\frac{\partial\mathfrak{V}}{\partial\theta}\right),\mathcal{E}_{\mathbb{z}\mathbb{z}}=\frac{\partial\mathfrak{W}}{\partial\mathbb{z}},\gamma_{\mathbb{r}\mathbb{z}}=\frac{\partial\mathfrak{U}}{\partial\mathbb{z}}+\frac{\partial\mathfrak{W}}{\partial\mathbb{r}},\\
&\gamma_{\mathbb{r}\theta}=\frac{1}{\mathbb{r}}\frac{\partial\mathfrak{U}}{\partial\theta}+\frac{\partial\mathfrak{V}}{\partial\mathbb{r}}-\frac{\mathfrak{V}}{\mathbb{r}},\gamma_{\theta\mathbb{z}}=\frac{\partial\mathfrak{V}}{\partial\mathbb{z}}+\frac{1}{\mathbb{r}}\frac{\partial\mathfrak{W}}{\partial\theta}.
\end{aligned}\tag{5}$$

Consequently, the non-zero strain parts regarding the core and piezoelectric layers can be specified as:

$$\mathcal{E}_{\mathbb{r}\mathbb{r}c}=\aleph^{(0)}_{\mathbb{r}\mathbb{r}c}+\mathbb{z}\aleph^{(1)}_{\mathbb{r}\mathbb{r}c}+\mathcal{T}(\mathbb{z})\aleph^{(2)}_{\mathbb{r}\mathbb{r}c}+g(\mathbb{z})\aleph^{(3)}_{\mathbb{r}\mathbb{r}c}+H(\mathbb{z})\aleph^{(4)}_{\mathbb{r}\mathbb{r}c},\tag{6a}$$

$$\mathcal{E}_{\theta\theta c}=\aleph^{(0)}_{\theta\theta c}+\mathbb{z}\aleph^{(1)}_{\theta\theta c}+\mathcal{T}(\mathbb{z})\aleph^{(2)}_{\theta\theta c}+g(\mathbb{z})\aleph^{(3)}_{\theta\theta c}+H(\mathbb{z})\aleph^{(4)}_{\theta\theta c},\tag{6b}$$

$$\mathcal{E}_{\mathbb{z}\mathbb{z}c}=\aleph^{(0)}_{\mathbb{z}\mathbb{z}c}+\mathbb{z}\aleph^{(1)}_{\mathbb{z}\mathbb{z}c}+\mathcal{T}(\mathbb{z})\aleph^{(2)}_{\mathbb{z}\mathbb{z}c}+g(\mathbb{z})\aleph^{(3)}_{\mathbb{z}\mathbb{z}c}+H(\mathbb{z})\aleph^{(4)}_{\mathbb{z}\mathbb{z}c},\tag{6c}$$

$$\gamma_{\theta\mathbb{z}c}=\aleph^{(0)}_{\theta\mathbb{z}c}+\mathbb{z}\aleph^{(1)}_{\theta\mathbb{z}c}+\mathcal{T}(\mathbb{z})\aleph^{(2)}_{\theta\mathbb{z}c}+g(\mathbb{z})\aleph^{(3)}_{\theta\mathbb{z}c}+H(\mathbb{z})\aleph^{(4)}_{\theta\mathbb{z}c},\tag{6d}$$

$$\gamma_{\mathbb{r}\mathbb{z}c}=\aleph^{(0)}_{\mathbb{r}\mathbb{z}c}+\mathbb{z}\aleph^{(1)}_{\mathbb{r}\mathbb{z}c}+\mathcal{T}(\mathbb{z})\aleph^{(2)}_{\mathbb{r}\mathbb{z}c}+g(\mathbb{z})\aleph^{(3)}_{\mathbb{r}\mathbb{z}c}+H(\mathbb{z})\aleph^{(4)}_{\mathbb{r}\mathbb{z}c},\tag{6e}$$

$$\gamma_{\mathbb{r}\theta c} = \aleph_{\mathbb{r}\theta c}^{(0)} + \mathbb{z}\aleph_{\mathbb{r}\theta c}^{(1)} + \mathcal{T}(\mathbb{z})\aleph_{\mathbb{r}\theta c}^{(2)} + g(\mathbb{z})\aleph_{\mathbb{r}\theta c}^{(3)} + H(\mathbb{z})\aleph_{\mathbb{r}\theta c}^{(4)}, \tag{6f}$$

$$\mathcal{E}_{\mathbb{r}\mathbb{r}p} = \aleph_{\mathbb{r}\mathbb{r}p}^{(0)} + \mathbb{z}\aleph_{\mathbb{r}\mathbb{r}p}^{(1)}, \tag{6g}$$

$$\mathcal{E}_{\theta\theta p} = \aleph_{\theta\theta p}^{(0)} + \mathbb{z}\aleph_{\theta\theta p}^{(1)}, \tag{6h}$$

$$\mathcal{E}_{\mathbb{z}\mathbb{z}p} = \aleph_{\mathbb{z}\mathbb{z}p}^{(0)} + \mathbb{z}\aleph_{\mathbb{z}\mathbb{z}p}^{(1)}, \tag{6i}$$

$$\gamma_{\theta\mathbb{z}p} = \aleph_{\theta\mathbb{z}p}^{(0)} + \mathbb{z}\aleph_{\theta\mathbb{z}p}^{(1)}, \tag{6j}$$

$$\gamma_{\mathbb{r}\mathbb{z}p} = \aleph_{\mathbb{r}\mathbb{z}p}^{(0)} + \mathbb{z}\aleph_{\mathbb{r}\mathbb{z}p}^{(1)}, \tag{6k}$$

$$\gamma_{\mathbb{r}\theta p} = \aleph_{\mathbb{r}\theta p}^{(0)} + \mathbb{z}\aleph_{\mathbb{r}\theta p}^{(1)}, \tag{6l}$$

where

$$\mathcal{E}_{\mathbb{r}\mathbb{r}c} = \frac{\partial\mathfrak{U}_{0c}}{\partial\mathbb{r}} + \mathbb{z}\alpha\frac{\partial^2\mathfrak{W}_{bc}}{\partial\mathbb{r}^2} + \mathbb{z}\beta\frac{\partial^2\mathfrak{W}_{sc}}{\partial\mathbb{r}^2} + \mathcal{T}(\mathbb{z})\frac{\partial^2\mathfrak{W}_{sc}}{\partial\mathbb{r}^2},$$
$$\aleph_{\mathbb{r}\mathbb{r}c}^{(0)} = \frac{\partial\mathfrak{U}_{0c}}{\partial\mathbb{r}}, \aleph_{\mathbb{r}\mathbb{r}c}^{(1)} = \alpha\frac{\partial^2\mathfrak{W}_{bc}}{\partial\mathbb{r}^2} + \beta\frac{\partial^2\mathfrak{W}_{sc}}{\partial\mathbb{r}^2},$$
$$\aleph_{\mathbb{r}\mathbb{r}c}^{(2)} = \frac{\partial^2\mathfrak{W}_{sc}}{\partial\mathbb{r}^2}, \aleph_{\mathbb{r}\mathbb{r}c}^{(3)} = 0, \aleph_{\mathbb{r}\mathbb{r}c}^{(4)} = 0,$$

$$\aleph_{\theta\theta c}^{(0)} = \frac{1}{\mathbb{r}}\left(\mathfrak{U}_{0c} + \frac{\partial\mathfrak{V}_{0c}}{\partial\theta}\right),$$
$$\aleph_{\theta\theta c}^{(1)} = \frac{1}{\mathbb{r}}\begin{pmatrix}\alpha\dfrac{\partial\mathfrak{W}_{bc}}{\partial\mathbb{r}} + \beta\dfrac{\partial\mathfrak{W}_{sc}}{\partial\mathbb{r}} \\ +\dfrac{\alpha}{\mathbb{r}}\dfrac{\partial^2\mathfrak{W}_{bc}}{\partial\theta^2} + \dfrac{\beta}{\mathbb{r}}\dfrac{\partial^2\mathfrak{W}_{sc}}{\partial\theta^2}\end{pmatrix},$$
$$\aleph_{\theta\theta c}^{(2)} = \frac{1}{\mathbb{r}}\left(\frac{\partial\mathfrak{W}_{sc}}{\partial\mathbb{r}} + \frac{1}{\mathbb{r}}\frac{\partial^2\mathfrak{W}_{sc}}{\partial\theta^2}\right), \aleph_{\theta\theta c}^{(3)} = 0, \aleph_{\theta\theta c}^{(4)} = 0,$$

$$\aleph_{\mathbb{z}\mathbb{z}c}^{(0)} = 0, \aleph_{\mathbb{z}\mathbb{z}c}^{(1)} = 0, \aleph_{\mathbb{z}\mathbb{z}c}^{(2)} = 0, \aleph_{\mathbb{z}\mathbb{z}c}^{(3)} = 0, \aleph_{\mathbb{z}\mathbb{z}c}^{(4)} = \mathfrak{W}_{sc},$$

$$\aleph_{\mathbb{r}\mathbb{z}c}^{(0)} = \alpha\frac{\partial\mathfrak{W}_{bc}}{\partial\mathbb{r}} + \beta\frac{\partial\mathfrak{W}_{sc}}{\partial\mathbb{r}} + \frac{\partial\mathfrak{W}_{bc}}{\partial\mathbb{r}}, \aleph_{\mathbb{r}\mathbb{z}c}^{(1)} = 0, \tag{7}$$
$$\aleph_{\mathbb{r}\mathbb{z}c}^{(2)} = 0, \aleph_{\mathbb{r}\mathbb{z}c}^{(3)} = 2\frac{\partial\mathfrak{W}_{sc}}{\partial\mathbb{r}} =, \aleph_{\mathbb{r}\mathbb{z}c}^{(4)} = 0,$$

$$\aleph_{\mathbb{r}\theta c}^{(0)} = \frac{1}{\mathbb{r}}\frac{\partial\mathfrak{U}_{0c}}{\partial\theta} + \frac{\partial\mathfrak{V}_{0c}}{\partial\mathbb{r}} - \frac{\mathfrak{V}_{0c}}{\mathbb{r}}, \aleph_{\mathbb{r}\theta c}^{(1)}$$
$$= \begin{pmatrix}\dfrac{\alpha}{\mathbb{r}}\dfrac{\partial^2\mathfrak{W}_{bc}}{\partial\mathbb{r}\partial\theta} + \dfrac{\beta}{\mathbb{r}}\dfrac{\partial^2\mathfrak{W}_{sc}}{\partial\mathbb{r}\partial\theta} - \dfrac{\alpha}{\mathbb{r}^2}\dfrac{\partial\mathfrak{W}_{bc}}{\partial\theta} + \dfrac{\alpha}{\mathbb{r}}\dfrac{\partial^2\mathfrak{W}_{bc}}{\partial\mathbb{r}\partial\theta} \\ -\dfrac{\beta}{\mathbb{r}^2}\dfrac{\partial\mathfrak{W}_{sc}}{\partial\theta} + \dfrac{\beta}{\mathbb{r}}\dfrac{\partial^2\mathfrak{W}_{sc}}{\partial\mathbb{r}\partial\theta} - \dfrac{\alpha}{\mathbb{r}^2}\dfrac{\partial\mathfrak{W}_{bc}}{\partial\theta} - \dfrac{\beta}{\mathbb{r}^2}\dfrac{\partial\mathfrak{W}_{sc}}{\partial\theta}\end{pmatrix},$$
$$\aleph_{\mathbb{r}\theta c}^{(2)} = \begin{pmatrix}\dfrac{\mathcal{T}(\mathbb{z})}{\mathbb{r}}\dfrac{\partial^2\mathfrak{W}_{sc}}{\partial\mathbb{r}\partial\theta} - \dfrac{\mathcal{T}(\mathbb{z})}{\mathbb{r}^2}\dfrac{\partial\mathfrak{W}_{sc}}{\partial\theta} \\ +\dfrac{\mathcal{T}(\mathbb{z})}{\mathbb{r}}\dfrac{\partial^2\mathfrak{W}_{sc}}{\partial\mathbb{r}\partial\theta} - \dfrac{\mathcal{T}(\mathbb{z})}{\mathbb{r}^2}\dfrac{\partial\mathfrak{W}_{sc}}{\partial\theta}\end{pmatrix},$$
$$\aleph_{\mathbb{r}\theta c}^{(3)} = 0, \aleph_{\mathbb{r}\theta c}^{(4)} = 0,$$

$$\aleph_{\theta\mathbb{z}c}^{(0)} = \alpha\frac{\partial\mathfrak{W}_{bc}}{\mathbb{r}\partial\theta} + \beta\frac{\partial\mathfrak{W}_{sc}}{\mathbb{r}\partial\theta} + \frac{\partial\mathfrak{W}_{bc}}{\mathbb{r}\partial\theta}, \aleph_{\theta\mathbb{z}c}^{(1)} =, \aleph_{\theta\mathbb{z}c}^{(2)} =$$

$$, \aleph_{\theta\mathbb{z}c}^{(3)} = 2g(\mathbb{z})\frac{\partial\mathfrak{W}_{sc}}{\mathbb{r}\partial\theta}, \aleph_{\theta\mathbb{z}c}^{(4)} = 0,$$

$$\aleph_{\mathbb{r}\mathbb{r}p}^{(0)} = 0, \aleph_{\mathbb{r}\mathbb{r}p}^{(1)} = -\frac{\partial^2\mathfrak{W}_{bc}}{\partial\mathbb{r}^2} - g\left(\frac{h_c}{2}\right)\frac{\partial^2\mathfrak{W}_{sc}}{\partial\mathbb{r}^2},$$

$$\aleph_{\theta\theta p}^{(0)} = 0, \aleph_{\theta\theta p}^{(1)} = \frac{1}{\mathbb{r}}\left(-\frac{\partial\mathfrak{W}_{bc}}{\partial\mathbb{r}} - g\left(\frac{h_c}{2}\right)\frac{\partial\mathfrak{W}_{sc}}{\partial\mathbb{r}} - \frac{1}{\mathbb{r}}\frac{\partial^2\mathfrak{W}_{bc}}{\partial\theta^2} - \frac{g\left(\frac{h_c}{2}\right)}{\mathbb{r}}\frac{\partial^2\mathfrak{W}_{sc}}{\partial\theta^2}\right),$$

$$\aleph_{\mathbb{z}\mathbb{z}p}^{(0)} = 0, \aleph_{\mathbb{z}\mathbb{z}p}^{(1)} = 0, \ , \ \aleph_{\theta\mathbb{z}p}^{(0)} = 0, \aleph_{\theta\mathbb{z}p}^{(1)} = 0,$$
$$\aleph_{\mathbb{r}\mathbb{z}p}^{(0)} = 0, \aleph_{\mathbb{r}\mathbb{z}p}^{(1)} = 0,$$

$$\aleph_{\mathbb{r}\theta p}^{(0)} = 0, \aleph_{\mathbb{r}\theta p}^{(1)} = -\frac{2}{\mathbb{r}}\frac{\partial^2\mathfrak{W}_{bc}}{\partial\mathbb{r}\partial\theta} - \frac{2}{\mathbb{r}}g\left(\frac{h_c}{2}\right)\frac{\partial^2\mathfrak{W}_{sc}}{\partial\mathbb{r}\partial\theta} + \frac{2}{\mathbb{r}^2}\frac{\partial\mathfrak{W}_{bc}}{\partial\theta} + \frac{2}{\mathbb{r}^2}g\left(\frac{h_c}{2}\right)\frac{\partial\mathfrak{W}_{sc}}{\partial\theta}.$$

where $H(\mathbb{z}) = \frac{\partial g(\mathbb{z})}{\partial\mathbb{z}}$. Also, a novel continuum approach known as nonlocal strain gradient elasticity accounts for the aforementioned phenomena (Lim *et al*. 2015)

$$\mathfrak{T}_{ij} - \mu^2\mathfrak{T}_{ij,mm} = C_{ijkl}\left(\mathcal{E}_{kl} - l^2\mathcal{E}_{kl,mm}\right), \tag{8}$$

Herein, the nonlocal factor (μ) expects the softening-stiffness process and the strain gradient factor (l) predicts the stiffness-strengthening system. In addition, $\mathfrak{T}_{ij}$ indicates a stress tensor and $\mathcal{E}_{ij}$ is a strain tensor, and the elastic moduli are indicated by C_{ijkl}.

By updating nonlocal strain gradient approach regarding the present scheme, the Eq. (8), for poroelastic system could be rewritten as follow

$$\begin{gathered}(1-\mu^2\nabla^2)\mathfrak{T}_{\mathbb{r}\mathbb{r}c} = (1-l^2\nabla^2)\left(\mathfrak{L}_{11c}\mathcal{E}_{\mathbb{r}\mathbb{r}c} + \mathfrak{L}_{12c}\mathcal{E}_{\theta\theta c} + \mathfrak{L}_{13c}\mathcal{E}_{\mathbb{z}\mathbb{z}c} - \gamma P_p\right), \\ (1-\mu^2\nabla^2)\mathfrak{T}_{\theta\theta c} = (1-l^2\nabla^2)\left(\mathfrak{L}_{12c}\mathcal{E}_{\mathbb{r}\mathbb{r}c} + \mathfrak{L}_{22c}\mathcal{E}_{\theta\theta c} + \mathfrak{L}_{23c}\mathcal{E}_{\mathbb{z}\mathbb{z}c} - \gamma P_p\right), \\ (1-\mu^2\nabla^2)\mathfrak{T}_{\mathbb{z}\mathbb{z}c} = (1-l^2\nabla^2)\left(\mathfrak{L}_{13c}\mathcal{E}_{\mathbb{r}\mathbb{r}c} + \mathfrak{L}_{23c}\mathcal{E}_{\theta\theta c} + \mathfrak{L}_{33c}\mathcal{E}_{\mathbb{z}\mathbb{z}c} - \gamma P_p\right), \\ (1-\mu^2\nabla^2)\mathfrak{T}_{\theta\mathbb{z}c} = (1-l^2\nabla^2)\mathfrak{L}_{44c}\gamma_{\theta\mathbb{z}c}, \\ (1-\mu^2\nabla^2)\mathfrak{T}_{\mathbb{r}\mathbb{z}c} = (1-l^2\nabla^2)\mathfrak{L}_{55c}\gamma_{\mathbb{r}\mathbb{z}c}, \\ (1-\mu^2\nabla^2)\mathfrak{T}_{\mathbb{r}\theta c} = (1-l^2\nabla^2)\mathfrak{L}_{66c}\gamma_{\mathbb{r}\theta c},\end{gathered} \tag{9}$$

where

$$\begin{gathered}\mathfrak{L}_{11c} = \frac{E(\mathbb{r},\theta,\mathbb{z},\mathbb{T})\left(1-\nu(\mathbb{r},\theta,\mathbb{z},\mathbb{T})\right)}{\left(1+\nu(\mathbb{r},\theta,\mathbb{z},\mathbb{T})\right)\left(1-2\nu(\mathbb{r},\theta,\mathbb{z},\mathbb{T})\right)}, \\ \mathfrak{L}_{33c} = \mathfrak{L}_{22c} = \mathfrak{L}_{11c}, \\ \mathfrak{L}_{12c} = \frac{E(\mathbb{r},\theta,\mathbb{z},\mathbb{T})\nu(\mathbb{r},\theta,\mathbb{z},\mathbb{T})}{\left(1+\nu(\mathbb{r},\theta,\mathbb{z},\mathbb{T})\right)\left(1-2\nu(\mathbb{r},\theta,\mathbb{z},\mathbb{T})\right)}, \\ \mathfrak{L}_{13c} = \mathfrak{L}_{23c} = \mathfrak{L}_{12c},\end{gathered} \tag{10}$$

$$\mathfrak{C}_{44c}=\frac{E(\mathbb{r},\theta,\mathbb{z},\mathbb{T})}{2\left(1+\nu(\mathbb{r},\theta,\mathbb{z},\mathbb{T})\right)},\mathfrak{C}_{66c}=\mathfrak{C}_{55c}=\mathfrak{C}_{44c}.$$

A definition of the material property P of 3D-PFG circular nanoplates in terms of the modified power-law is as follows:

$$E(\mathbb{r},\theta,\mathbb{z},\mathbb{T})=E_m+(E_c-E_m)\left(0.5+\frac{\mathbb{z}}{h}\right)^{n_{\mathbb{z}}}\left(\frac{\mathbb{r}}{R_o}\right)^{n_{\mathbb{r}}}\left(\frac{\theta}{\theta_m}\right)^{n_\theta}. \tag{11a}$$

$$\nu(\mathbb{r},\theta,\mathbb{z},\mathbb{T})=\nu_m+(\nu_c-\nu_m)\left(0.5+\frac{\mathbb{z}}{h}\right)^{n_{\mathbb{z}}}\left(\frac{\mathbb{r}}{R_o}\right)^{n_{\mathbb{r}}}\left(\frac{\theta}{\theta_m}\right)^{n_\theta}. \tag{11b}$$

$$\alpha(\mathbb{r},\theta,\mathbb{z},\mathbb{T})=\alpha_m+(\alpha_c-\alpha_m)\left(0.5+\frac{\mathbb{z}}{h}\right)^{n_{\mathbb{z}}}\left(\frac{\mathbb{r}}{R_o}\right)^{n_{\mathbb{r}}}\left(\frac{\theta}{\theta_m}\right)^{n_\theta}. \tag{11c}$$

The FGMs, the neutral plane is not by the side of the mid-plane (Barretta *et al*. 2016) though the authors assume this in our study.

The other factor related to Eq. (9) are reported by (Liu *et al*. 2022)

$$P_p=\frac{\psi-(\mathcal{E}_{\mathbb{r}\mathbb{r}}+\mathcal{E}_{\theta\theta}+\mathcal{E}_{\mathbb{z}\mathbb{z}})}{(K^P)^{-1}} \tag{12a}$$

$$K^P=-(k_t-k_{\mathfrak{U}})\gamma^{-2} \tag{12b}$$

$$k_{\mathfrak{U}}=\left[1-\frac{k_{\mathcal{T}}\gamma^2}{(\phi-\gamma)(1-\gamma)k_{\mathcal{T}}+k_{\mathcal{T}}\phi}\right]k_t \tag{12c}$$

Undrained fluid conditions are represented by $\psi=0$ in Eq. (12a), which results in:

$$P_p=-K^P\gamma\mathcal{E}=-K^P(\mathcal{E}_{\mathbb{r}\mathbb{r}}+\mathcal{E}_{\theta\theta}+\mathcal{E}_{\mathbb{z}\mathbb{z}})\gamma. \tag{13}$$

Putting in Eq. (13) for the solution of Eq. (9) yields

$$\begin{gathered}
(1-\mu^2\nabla^2)\mathfrak{T}_{\mathbb{r}\mathbb{r}c}=(1-l^2\nabla^2)(\overline{\mathfrak{C}}_{11c}\mathcal{E}_{\mathbb{r}\mathbb{r}c}+\overline{\mathfrak{C}}_{12}\mathcal{E}_{\theta\theta c}+\overline{\mathfrak{C}}_{13}\mathcal{E}_{\mathbb{z}\mathbb{z}c}),\\
(1-\mu^2\nabla^2)\mathfrak{T}_{\theta\theta c}=(1-l^2\nabla^2)(\overline{\mathfrak{C}}_{12c}\mathcal{E}_{\mathbb{r}\mathbb{r}c}+\overline{\mathfrak{C}}_{22c}\mathcal{E}_{\theta\theta c}+\overline{\mathfrak{C}}_{23c}\mathcal{E}_{\mathbb{z}\mathbb{z}c}),\\
(1-\mu^2\nabla^2)\mathfrak{T}_{\mathbb{z}\mathbb{z}c}=(1-l^2\nabla^2)(\overline{\mathfrak{C}}_{13c}\mathcal{E}_{\mathbb{r}\mathbb{r}c}+\overline{\mathfrak{C}}_{23c}\mathcal{E}_{\theta\theta c}+\overline{\mathfrak{C}}_{33c}\mathcal{E}_{\mathbb{z}\mathbb{z}c}),\\
(1-\mu^2\nabla^2)\mathfrak{T}_{\theta\mathbb{z}c}=(1-l^2\nabla^2)\overline{\mathfrak{C}}_{44c}\gamma_{\theta\mathbb{z}c},\\
(1-\mu^2\nabla^2)\mathfrak{T}_{\mathbb{r}\mathbb{z}c}=(1-l^2\nabla^2)\overline{\mathfrak{C}}_{55c}\gamma_{\mathbb{r}\mathbb{z}c},\\
(1-\mu^2\nabla^2)\mathfrak{T}_{\mathbb{r}\theta c}=(1-l^2\nabla^2)\overline{\mathfrak{C}}_{66c}\gamma_{\mathbb{r}\theta},
\end{gathered} \tag{14}$$

where

$$\begin{gathered}
\bar{\mathfrak{C}}_{ijc}=\mathfrak{C}_{ijc}+K\gamma^2 i,j=1,2,3.\\
\bar{\mathfrak{C}}_{ijc}=\mathfrak{C}_{ijc} i=j=4,5,6.
\end{gathered} \tag{15}$$

Piezoelectric layer constitutive equations are derived by:

$$\begin{gathered}
(1-\mu^2\nabla^2)\mathfrak{T}_{\mathbb{r}\mathbb{r}p}=(1-l^2\nabla^2)\left(\mathfrak{C}_{11p}\mathcal{E}_{\mathbb{r}\mathbb{r}p}+\mathfrak{C}_{12p}\mathcal{E}_{\theta\theta p}-e_{31p}E_{\mathbb{z}}\right),\\
(1-\mu^2\nabla^2)\mathfrak{T}_{\theta\theta p}=(1-l^2\nabla^2)\left(\mathfrak{C}_{12p}\mathcal{E}_{\mathbb{r}\mathbb{r}p}+\mathfrak{C}_{22p}\mathcal{E}_{\theta\theta p}-e_{32p}E_{\mathbb{z}}\right),\\
(1-\mu^2\nabla^2)\mathfrak{T}_{\theta\mathbb{z}p}=(1-l^2\nabla^2)\left(\mathfrak{C}_{44p}\gamma_{\theta\mathbb{z}p}-e_{24p}E_\theta\right),\\
(1-\mu^2\nabla^2)\mathfrak{T}_{\mathbb{r}\mathbb{z}p}=(1-l^2\nabla^2)\left(\mathfrak{C}_{55p}\gamma_{\mathbb{r}\mathbb{z}p}-e_{15p}E_{\mathbb{r}}\right),\\
(1-\mu^2\nabla^2)\mathfrak{T}_{\mathbb{r}\theta p}=(1-l^2\nabla^2)\left(\mathfrak{C}_{66p}\gamma_{\mathbb{r}\theta p}\right),
\end{gathered} \tag{16}$$

The electric displacement relations are developed as

$$\begin{gathered}
(1-\mu^2\nabla^2)\mathbb{D}_{\mathbb{r}p}=(1-l^2\nabla^2)\left(e_{15p}\gamma_{\mathbb{r}\mathbb{z}p}+\eta_{11p}E_{\mathbb{r}}\right),\\
(1-\mu^2\nabla^2)\mathbb{D}_{\theta p}=(1-l^2\nabla^2)\left(e_{15p}\gamma_{\theta\mathbb{z}p}+\eta_{22p}E_\theta\right),\\
(1-\mu^2\nabla^2)\mathbb{D}_{\mathbb{z}p}=(1-l^2\nabla^2)\left(e_{31p}\mathcal{E}_{\mathbb{r}\mathbb{r}p}+e_{32p}\mathcal{E}_{\theta\theta p}+\eta_{33p}E_{\mathbb{z}}\right),
\end{gathered} \tag{17}$$

where (Gholami and Ansari 2017)

$$\begin{gathered}
\mathfrak{C}_{11p}=\mathfrak{C}_{11}-\frac{\mathfrak{C}_{13}^2}{\mathfrak{C}_{33}},\ \mathfrak{C}_{12p}=\mathfrak{C}_{12}-\frac{\mathfrak{C}_{13}\mathfrak{C}_{23}}{\mathfrak{C}_{33}},\ \mathfrak{C}_{22p}=\mathfrak{C}_{22}-\frac{\mathfrak{C}_{23}^2}{\mathfrak{C}_{33}},\\
\mathfrak{C}_{44p}=\mathfrak{C}_{44},\ \mathfrak{C}_{55p}=\mathfrak{C}_{55},\ \mathfrak{C}_{66p}=\mathfrak{C}_{66},\\
e_{31p}=e_{31}-\frac{\mathfrak{C}_{13}e_{33}}{\mathfrak{C}_{33}},\quad e_{32p}=e_{32}-\frac{\mathfrak{C}_{23}e_{33}}{\mathfrak{C}_{33}},\ e_{15p}=e_{15},\ e_{24p}=e_{24},\\
\eta_{11p}=\eta_{11},\ \eta_{22p}=\eta_{22},\ \eta_{33p}=\eta_{33}+\frac{e_{33}^2}{\mathfrak{C}_{33}},
\end{gathered} \tag{18}$$

Corresponding electric domain strength i.e. $E_{\mathbb{r}},\ E_\theta,\ E_{\mathbb{z}}$, which can be joined to Eqs. (16), (17), are expressed by:

$$E_{\mathbb{r}}=-\frac{\partial\psi}{\partial\mathbb{r}},\ E_\theta=-\frac{1}{\mathbb{r}}\frac{\partial\psi}{\partial\theta},\ E_{\mathbb{z}}=-\frac{\partial\psi}{\partial\mathbb{z}} \tag{19}$$

Ke and Wang (2014) surveyed that the electric potential $\psi(\mathbb{r},\theta,\mathbb{z},t)$ is determined by

$$\psi(\mathbb{r},\theta,\mathbb{z},t)=-cos(\beta\mathbb{z})\,\phi(\mathbb{r},\theta,t)+\frac{2\mathbb{z}\phi_0}{h} \tag{20}$$

Herein, ϕ_0 and $\beta=\pi/h$ indicate the initial outward electric. Extra, $\phi(\mathbb{r},\theta,t)$ denotes a spatial difference regarding the electric potential regarding the axes associated with *r* and θ.

2.3 Minimum total potential energy

Now, using the least overall potential energy concept, it is possible to write: (Yaghoobi and Torabi 2013)

$$\delta\left((\mathit{\Pi}_{\mathbb{T}}+\mathit{\Pi}_{\mathfrak{WB}})\text{-}\mathit{\Pi}_e\right)=0 \tag{21}$$

The energy term in the above relation are expressed as below:

$$\Pi_e = \int\{\sigma_{rrc}\varepsilon_{rrc} + \sigma_{\theta\theta c}\varepsilon_{\theta\theta c} + \sigma_{zzc}\varepsilon_{zzc} + \tau_{rzc}\gamma_{rzc} + \tau_{\theta zc}\gamma_{\theta zc} + \tau_{r\theta c}\gamma_{r\theta c}\}dV + \int\left(\sigma_{rrp}\varepsilon_{rrp} + \sigma_{\theta\theta p}\varepsilon_{\theta\theta p} + \sigma_{zzp}\varepsilon_{zzp} + \tau_{\theta zp}\gamma_{\theta zp} + \tau_{rzp}\gamma_{rzp} + \tau_{r\theta p}\gamma_{r\theta p} - D_{rp}E_{rp} - D_{\theta p}E_{\theta p} - D_{zp}E_{zp}\right)dV, \quad (22a)$$

$$\Pi_T = \frac{1}{2}\int\left\{\frac{N_T}{r}\frac{\partial}{\partial r}\left(r\frac{\partial w_{0c}}{\partial r}\right) + \frac{N_T}{r^2}\frac{\partial^2 w_{0c}}{\partial\theta^2}\right\}w_{0c}dA. \quad (22b)$$

The first variant of the work performed in response to an externally implemented electric force:

$$\Pi_{\mathfrak{W}} = \frac{1}{2}\int N_p\left(\frac{1}{\mathbb{r}}\frac{\partial}{\partial\mathbb{r}}\left(\mathbb{r}\frac{\partial\mathfrak{W}_{0c}}{\partial\mathbb{r}}\right) + \frac{1}{\mathbb{r}^2}\frac{\partial^2\mathfrak{W}_{0c}}{\partial\theta^2}\right)\mathfrak{W}_{0c}dA \quad (23)$$

The electric load determined by (SafarPour *et al.* 2019):

$$\mathfrak{N}_P = -2\left(e_{31} - \frac{\mathfrak{L}_{13}e_{33}}{\mathfrak{L}_{33}}\right)\phi_0 \quad (24)$$

By replacement of Eqs. (22a-b), and (23) into Eq. (21), the following relations result from a mathematical calculation.

$$\delta u_{0c}: \frac{1}{r}\frac{\partial(rN_{rrc})}{\partial r} - \frac{N_{\theta\theta c}}{r} + \frac{\partial N_{r\theta c}}{r\partial\theta} = 0, \quad (25a)$$

$$\delta v_{0c}: \frac{1}{r}\frac{\partial N_{\theta\theta c}}{\partial\theta} + \frac{1}{r}\frac{\partial(rN_{r\theta c})}{\partial r} + \frac{N_{r\theta c}}{r} = 0, \quad (25b)$$

$$\delta w_{0c}: \frac{1}{r}\frac{\partial^2(rM_{rrc})}{\partial r^2} - \frac{1}{r}\frac{\partial M_{\theta\theta c}}{\partial r} + \frac{1}{r^2}\frac{\partial^2 M_{\theta\theta c}}{\partial\theta^2} + \frac{2}{r}\frac{\partial^2 M_{r\theta c}}{\partial r\partial\theta} + \frac{2}{r^2}\frac{\partial M_{r\theta c}}{\partial\theta} + \frac{1}{r}\frac{\partial^2(rM_{rrp})}{\partial r^2} - \frac{1}{r}\frac{\partial M_{\theta\theta p}}{\partial r} + \frac{1}{r^2}\frac{\partial^2 M_{\theta\theta p}}{\partial\theta^2} + \frac{2}{r}\frac{\partial^2 M_{r\theta p}}{\partial r\partial\theta} + \frac{2}{r^2}\frac{\partial M_{r\theta p}}{\partial\theta} - N_p\nabla^2 w_{0c} = N_T\nabla^2 w_{0c}, \quad (25c)$$

$$\delta w_{1c}: -\frac{1}{r}\frac{\partial^2(rP_{rrc})}{\partial r^2} + \frac{1}{r}\frac{\partial P_{\theta\theta c}}{\partial r} - \frac{1}{r^2}\frac{\partial^2 P_{\theta\theta c}}{\partial\theta^2} - R_{zzc} + \frac{2}{r}\frac{\partial(rQ_{rzc})}{\partial r} + \frac{2}{r}\frac{\partial Q_{\theta zc}}{\partial\theta} - \frac{2}{r}\frac{\partial^2 P_{r\theta c}}{\partial r\partial\theta} - \frac{2}{r^2}\frac{\partial P_{r\theta c}}{\partial\theta} + \frac{g\left(\frac{h_c}{2}\right)}{r}\frac{\partial^2(rM_{rrp})}{\partial r^2} - \frac{g\left(\frac{h_c}{2}\right)}{r}\frac{\partial M_{\theta\theta p}}{\partial r} + \frac{g\left(\frac{h_c}{2}\right)}{r^2}\frac{\partial^2 M_{\theta\theta p}}{\partial\theta^2} + \frac{2g\left(\frac{h_c}{2}\right)}{r}\frac{\partial^2 M_{r\theta p}}{\partial r\partial\theta} + \frac{2g\left(\frac{h_c}{2}\right)}{r^2}\frac{\partial M_{r\theta p}}{\partial\theta} = 0, \quad (25d)$$

$$\delta\phi: \int_V\left\{\frac{1}{r}\frac{\partial(rD_r)}{\partial r}cos(\beta z) + \frac{\partial D_\theta}{r\partial\theta}cos(\beta z) + \beta D_z\,sin(\beta z)\right\}dV = 0, \quad (25e)$$

The associated BCs can be specified by

$$\delta u_{0c} = 0 \quad \text{or} \quad (N_{rrc})\hat{n}_r + \left(\frac{N_{r\theta c}}{r}\right)\hat{n}_\theta = 0, \quad (26a)$$

$$\delta v_{0c} = 0 \quad \text{or} \quad (N_{r\theta c})\hat{n}_r + \left(\frac{N_{\theta\theta c}}{r}\right)\hat{n}_\theta = 0, \quad (26b)$$

$$\delta w_{0c} = 0 \quad \text{or} \quad \left\{\frac{\partial(rM_{rrc})}{r\partial r} - \frac{M_{\theta\theta c}}{r} + 2\frac{\partial M_{r\theta c}}{r\partial\theta} + \frac{\partial(rM_{rrp})}{r\partial r} - \frac{M_{\theta\theta p}}{r} + \frac{\partial M_{r\theta p}}{r\partial\theta}\right\}\hat{n}_r + \left\{\frac{\partial M_{\theta\theta c}}{r^2\partial\theta} + \frac{M_{r\theta c}}{r^2} - \frac{\partial M_{r\theta c}}{r^2\partial\theta} + \frac{\partial M_{\theta\theta p}}{r^2\partial\theta} + \frac{\partial M_{r\theta p}}{r\partial r} + \frac{2M_{r\theta p}}{r^2}\right\}\hat{n}_\theta = 0\,, \quad (26c)$$

$$\delta w_{1c} = 0 \quad \text{or} \quad \left(\frac{\partial(rP_{rrc})}{r\partial r} - \frac{P_{\theta\theta c}}{r} - 2N_{rzc} + \frac{\partial P_{r\theta c}}{r\partial\theta} + g\left(\frac{h_c}{2}\right)\frac{\partial(rM_{rrp})}{r\partial r} - g\left(\frac{h_c}{2}\right)\frac{M_{\theta\theta p}}{r} + g\left(\frac{h_c}{2}\right)\frac{\partial M_{r\theta p}}{r\partial\theta}\right)\hat{n}_r + \left(\frac{\partial P_{\theta\theta c}}{r^2\partial\theta} - \frac{2}{r}N_{\theta zc} + \frac{2P_{r\theta c}}{r^2} + \frac{\partial P_{r\theta c}}{r\partial r} + g\left(\frac{h_c}{2}\right)\frac{\partial M_{\theta\theta p}}{r^2\partial\theta} + g\left(\frac{h_c}{2}\right)\frac{\partial M_{r\theta p}}{r\partial r} + g\left(\frac{h_c}{2}\right)\frac{2M_{r\theta p}}{r^2}\right)\hat{n}_\theta = 0\,, \quad (26d)$$

$$\frac{\partial\delta w_{0c}}{\partial r} = 0 \quad \text{or} \quad \left(M_{rrc} + M_{rrp}\right)\hat{n}_r + \left(\frac{M_{r\theta c}}{r} + \frac{M_{r\theta p}}{r}\right)\hat{n}_\theta = 0, \quad (26e)$$

$$\frac{\partial\delta w_{0c}}{\partial\theta} = 0 \quad \text{or} \quad \left(\frac{M_{r\theta c}}{r} + \frac{M_{r\theta p}}{r}\right)\hat{n}_r + \left(\frac{M_{\theta\theta c}}{r^2} + \frac{M_{\theta\theta p}}{r^2}\right)\hat{n}_\theta = 0, \quad (26f)$$

$$\frac{\partial\delta w_{1c}}{\partial r} = 0 \quad \text{or} \quad \left(P_{rrc} + g\left(\frac{h_c}{2}\right)M_{rrp}\right)\hat{n}_r + \left(\frac{P_{r\theta c}}{r} + g\left(\frac{h_c}{2}\right)\frac{M_{r\theta p}}{r}\right)\hat{n}_\theta = 0, \quad (26g)$$

$$\frac{\partial\delta w_{1c}}{\partial\theta} = 0 \quad \text{or} \quad \left(\frac{P_{r\theta c}}{r} + g\left(\frac{h_c}{2}\right)\frac{M_{r\theta p}}{r}\right)\hat{n}_r + \left(\frac{P_{\theta\theta c}}{r^2} + g\left(\frac{h_c}{2}\right)\frac{M_{\theta\theta p}}{r^2}\right)\hat{n}_\theta = 0, \quad (26h)$$

$$\delta\phi = 0. \quad (26i)$$

where

$$\begin{gathered}
\mathfrak{N}_{\mathbb{r}\mathbb{r}c} = \int_V \mathfrak{T}_{\mathbb{r}\mathbb{r}c}\mathbb{r}d\mathbb{r}d\theta d\mathbb{z}, \\
\mathfrak{M}_{\mathbb{r}\mathbb{r}c} = \int_V \mathbb{z}\times\mathfrak{T}_{\mathbb{r}\mathbb{r}c}\mathbb{r}d\mathbb{r}d\theta d\mathbb{z}, \\
\mathfrak{P}_{\mathbb{r}\mathbb{r}c} = \int_V \mathcal{T}(\mathbb{z})\times\mathfrak{T}_{\mathbb{r}\mathbb{r}c}\mathbb{r}d\mathbb{r}d\theta d\mathbb{z}, \\
\mathfrak{L}_{\mathbb{r}\mathbb{r}c} = \int_V g(\mathbb{z})\times\mathfrak{T}_{\mathbb{r}\mathbb{r}c}\mathbb{r}d\mathbb{r}d\theta d\mathbb{z}, \\
\mathfrak{R}_{\mathbb{r}\mathbb{r}c} = \int_V H(\mathbb{z})\times\mathfrak{T}_{\mathbb{r}\mathbb{r}c}\mathbb{r}d\mathbb{r}d\theta d\mathbb{z}, \\
\mathfrak{N}_{\theta\theta c} = \int_V \mathfrak{T}_{\theta\theta c}\mathbb{r}d\mathbb{r}d\theta d\mathbb{z}, \\
\mathfrak{M}_{\theta\theta c} = \int_V \mathbb{z}\times\mathfrak{T}_{\mathbb{r}\mathbb{r}c}\mathbb{r}d\mathbb{r}d\theta d\mathbb{z}, \\
\mathfrak{P}_{\theta\theta c} = \int_V \mathcal{T}(\mathbb{z})\times\mathfrak{T}_{\theta\theta c}\mathbb{r}d\mathbb{r}d\theta d\mathbb{z}, \qquad (27) \\
\mathfrak{L}_{\theta\theta c} = \int_V g(\mathbb{z})\times\mathfrak{T}_{\theta\theta c}\mathbb{r}d\mathbb{r}d\theta d\mathbb{z}, \\
\mathfrak{R}_{\theta\theta c} = \int_V H(\mathbb{z})\times\mathfrak{T}_{\theta\theta c}\mathbb{r}d\mathbb{r}d\theta d\mathbb{z}, \\
\mathfrak{N}_{\mathbb{z}\mathbb{z}c} = \int_V \mathfrak{T}_{\mathbb{z}\mathbb{z}c}\mathbb{r}d\mathbb{r}d\theta d\mathbb{z}, \\
\mathfrak{M}_{\mathbb{z}\mathbb{z}c} = \int_V \mathbb{z}\times\mathfrak{T}_{\mathbb{z}\mathbb{z}c}\mathbb{r}d\mathbb{r}d\theta d\mathbb{z}, \\
\mathfrak{P}_{\mathbb{z}\mathbb{z}c} = \int_V \mathcal{T}(\mathbb{z})\times\mathfrak{T}_{\mathbb{z}\mathbb{z}c}\mathbb{r}d\mathbb{r}d\theta d\mathbb{z}, \\
\mathfrak{L}_{\mathbb{z}\mathbb{z}c} = \int_V g(\mathbb{z})\times\mathfrak{T}_{\mathbb{z}\mathbb{z}c}\mathbb{r}d\mathbb{r}d\theta d\mathbb{z}, \\
\mathfrak{R}_{\mathbb{z}\mathbb{z}c} = \int_V H(\mathbb{z})\times\mathfrak{T}_{\mathbb{z}\mathbb{z}c}\mathbb{r}d\mathbb{r}d\theta d\mathbb{z},
\end{gathered}$$

$$\mathfrak{N}_{\theta\mathbb{z}c}=\int_V \mathfrak{T}_{\theta\mathbb{z}c}\mathbb{r}d\mathbb{r}d\theta d\mathbb{z},$$

$$\mathfrak{M}_{\theta\mathbb{z}c}=\int_V \mathbb{z}\times\mathfrak{T}_{\theta\mathbb{z}c}\mathbb{r}d\mathbb{r}d\theta d\mathbb{z},$$

$$\mathfrak{P}_{\theta\mathbb{z}c}=\int_V \mathcal{T}(\mathbb{z})\times\mathfrak{T}_{\theta\mathbb{z}c}\mathbb{r}d\mathbb{r}d\theta d\mathbb{z},$$

$$\mathfrak{L}_{\theta\mathbb{z}c}=\int_V g(\mathbb{z})\times\mathfrak{T}_{\theta\mathbb{z}c}\mathbb{r}d\mathbb{r}d\theta d\mathbb{z},$$

$$\mathfrak{R}_{\theta\mathbb{z}c}=\int_V H(\mathbb{z})\times\mathfrak{T}_{\theta\mathbb{z}c}\mathbb{r}d\mathbb{r}d\theta d\mathbb{z},$$

$$\mathfrak{N}_{\mathbb{r}\mathbb{z}c}=\int_V \mathfrak{T}_{\mathbb{r}\mathbb{z}c}\mathbb{r}d\mathbb{r}d\theta d\mathbb{z},$$

$$\mathfrak{M}_{\mathbb{r}\mathbb{z}c}=\int_V \mathbb{z}\times\mathfrak{T}_{\mathbb{r}\mathbb{z}c}\mathbb{r}d\mathbb{r}d\theta d\mathbb{z},$$

$$\mathfrak{P}_{\mathbb{r}\mathbb{z}c}=\int_V \mathcal{T}(\mathbb{z})\times\mathfrak{T}_{\mathbb{r}\mathbb{z}c}\mathbb{r}d\mathbb{r}d\theta d\mathbb{z},$$

$$\mathfrak{L}_{\mathbb{r}\mathbb{z}c}=\int_V g(\mathbb{z})\times\mathfrak{T}_{\mathbb{r}\mathbb{z}c}\mathbb{r}d\mathbb{r}d\theta d\mathbb{z},$$

$$\mathfrak{R}_{\mathbb{r}\mathbb{z}c}=\int_V H(\mathbb{z})\times\mathfrak{T}_{\mathbb{r}\mathbb{z}c}\mathbb{r}d\mathbb{r}d\theta d\mathbb{z},$$

$$\mathfrak{N}_{\mathbb{r}\theta c}=\int_V \mathfrak{T}_{\mathbb{r}\theta c}\mathbb{r}d\mathbb{r}d\theta d\mathbb{z},$$

$$\mathfrak{M}_{\mathbb{r}\theta c}=\int_V \mathbb{z}\times\mathfrak{T}_{\mathbb{r}\theta c}\mathbb{r}d\mathbb{r}d\theta d\mathbb{z},$$

$$\mathfrak{P}_{\mathbb{r}\theta c}=\int_V \mathcal{T}(\mathbb{z})\times\mathfrak{T}_{\mathbb{r}\theta c}\mathbb{r}d\mathbb{r}d\theta d\mathbb{z},$$

$$\mathfrak{L}_{\mathbb{r}\theta c}=\int_V g(\mathbb{z})\times\mathfrak{T}_{\mathbb{r}\theta c}\mathbb{r}d\mathbb{r}d\theta d\mathbb{z},$$

$$\mathfrak{R}_{\mathbb{r}\theta c}=\int_V H(\mathbb{z})\times\mathfrak{T}_{\mathbb{r}\theta c}\mathbb{r}d\mathbb{r}d\theta d\mathbb{z},$$

$$\mathfrak{N}_{\mathbb{r}\mathbb{r}p}=\int_V \mathfrak{T}_{\mathbb{r}\mathbb{r}p}\mathbb{r}d\mathbb{r}d\theta d\mathbb{z},$$

$$\mathfrak{N}_{\theta\theta p}=\int_V \mathfrak{T}_{\theta\theta p}\mathbb{r}d\mathbb{r}d\theta d\mathbb{z},$$

$$\mathfrak{N}_{\mathbb{z}\mathbb{z}p}=\int_V \mathfrak{T}_{\mathbb{z}\mathbb{z}p}\mathbb{r}d\mathbb{r}d\theta d\mathbb{z},$$

$$\mathfrak{M}_{\mathbb{r}\mathbb{r}p}=\int_V \mathbb{z}\times\mathfrak{T}_{\mathbb{r}\mathbb{r}p}\mathbb{r}d\mathbb{r}d\theta d\mathbb{z},$$

$$\mathfrak{M}_{\theta\theta p}=\int_V \mathbb{z}\times\mathfrak{T}_{\theta\theta p}\mathbb{r}d\mathbb{r}d\theta d\mathbb{z},$$

$$\mathfrak{M}_{\mathbb{z}\mathbb{z}p}=\int_V \mathbb{z}\times\mathfrak{T}_{\mathbb{z}\mathbb{z}p}\mathbb{r}d\mathbb{r}d\theta d\mathbb{z},$$

$$\mathfrak{N}_{\theta\mathbb{z}p}=\int_V \mathfrak{T}_{\theta\mathbb{z}p}\mathbb{r}d\mathbb{r}d\theta d\mathbb{z},$$

$$\mathfrak{N}_{\mathbb{r}\mathbb{z}p}=\int_V \mathfrak{T}_{\mathbb{r}\mathbb{z}p}\mathbb{r}d\mathbb{r}d\theta d\mathbb{z},$$

$$\mathfrak{N}_{\mathbb{r}\theta p}=\int_V \mathfrak{T}_{\mathbb{r}\theta p}\mathbb{r}d\mathbb{r}d\theta d\mathbb{z},$$

$$\mathfrak{M}_{\theta\mathbb{z}p}=\int_V \mathbb{z}\times\mathfrak{T}_{\theta\mathbb{z}p}\mathbb{r}d\mathbb{r}d\theta d\mathbb{z},$$

$$\mathfrak{M}_{\mathbb{r}\mathbb{z}p}=\int_V \mathbb{z}\times\mathfrak{T}_{\mathbb{r}\mathbb{z}p}\mathbb{r}d\mathbb{r}d\theta d\mathbb{z},$$

$$\mathfrak{M}_{\mathbb{r}\theta p}=\int_V \mathbb{z}\times\mathfrak{T}_{\mathbb{r}\theta p}\mathbb{r}d\mathbb{r}d\theta d\mathbb{z}.$$

Replacement related to Eqs. (14), (16), and (17) into Eqs. (25a)-(25e), regarding the universal nonlocal strain gradient refined shear deformable scheme, the equations of motion for the 3D-PFG reinforced nanplate are presented in terms of displacement fields:

$$\delta u_{0c}\colon (1-\ell^2\nabla^2)\left(\frac{1}{r}\frac{\partial(rN_{rrc})}{\partial r}-\frac{N_{\theta\theta c}}{r}+\frac{\partial N_{r\theta c}}{r\partial\theta}\right)=0, \quad (28a)$$

$$\delta v_{0c}\colon (1-\ell^2\nabla^2)\left(\frac{1}{r}\frac{\partial N_{\theta\theta c}}{\partial\theta}+\frac{1}{r}\frac{\partial(rN_{r\theta c})}{\partial r}+\frac{N_{r\theta c}}{r}\right)= 0, \quad (28b)$$

$$\begin{aligned}\delta w_{0c}\colon\ (1-\ell^2\nabla^2)\Bigg(&\frac{1}{r}\frac{\partial^2(rM_{rrc})}{\partial r^2}-\frac{1}{r}\frac{\partial M_{\theta\theta c}}{\partial r}+\\ &\frac{1}{r^2}\frac{\partial^2 M_{\theta\theta c}}{\partial\theta^2}+\frac{2}{r}\frac{\partial^2 M_{r\theta c}}{\partial r\partial\theta}+\frac{2}{r^2}\frac{\partial M_{r\theta c}}{\partial\theta}+\frac{1}{r}\frac{\partial^2(rM_{rrp})}{\partial r^2}-\\ &\frac{1}{r}\frac{\partial M_{\theta\theta p}}{\partial r}+\frac{1}{r^2}\frac{\partial^2 M_{\theta\theta p}}{\partial\theta^2}+\frac{2}{r}\frac{\partial^2 M_{r\theta p}}{\partial r\partial\theta}+\frac{2}{r^2}\frac{\partial M_{r\theta p}}{\partial\theta}\Bigg)-\\ &(1-\mu^2\nabla^2)N_p\nabla^2 w_{0c}=(1-\mu^2\nabla^2)N_T\nabla^2 w_{0c},\end{aligned} \quad (28c)$$

$$\begin{aligned}\delta w_{1c}\colon\ (1-\ell^2\nabla^2)\Bigg(&-\frac{1}{r}\frac{\partial^2(rP_{rrc})}{\partial r^2}+\frac{1}{r}\frac{\partial P_{\theta\theta c}}{\partial r}-\\ &\frac{1}{r^2}\frac{\partial^2 P_{\theta\theta c}}{\partial\theta^2}-R_{zzc}+\frac{2}{r}\frac{\partial(rQ_{rzc})}{\partial r}+\frac{2}{r}\frac{\partial Q_{\theta zc}}{\partial\theta}-\frac{2}{r}\frac{\partial^2 P_{r\theta c}}{\partial r\partial\theta}-\\ &\frac{2}{r^2}\frac{\partial P_{r\theta c}}{\partial\theta}+\frac{g\left(\frac{h_c}{2}\right)}{r}\frac{\partial^2(rM_{rrp})}{\partial r^2}-\frac{g\left(\frac{h_c}{2}\right)}{r}\frac{\partial M_{\theta\theta p}}{\partial r}+\\ &\frac{g\left(\frac{h_c}{2}\right)}{r^2}\frac{\partial^2 M_{\theta\theta p}}{\partial\theta^2}+\frac{2g\left(\frac{h_c}{2}\right)}{r}\frac{\partial^2 M_{r\theta p}}{\partial r\partial\theta}+\frac{2g\left(\frac{h_c}{2}\right)}{r^2}\frac{\partial M_{r\theta p}}{\partial\theta}\Bigg)=0,\end{aligned} \quad (28d)$$

$$\begin{aligned}\delta\phi\colon\ \int_V(1-\ell^2\nabla^2)\Bigg\{&\frac{1}{r}\frac{\partial(rD_r)}{\partial r}cos(\beta z)+\\ &\frac{\partial D_\theta}{r\partial\theta}cos(\beta z)+\beta D_z\,sin(\beta z)\Bigg\}dV=0,\end{aligned} \quad (28e)$$

3. Solution procedure

The HDQ and DQ techniques are designed to estimate the partial derivatives related to a function regarding a spatial parameter by the side of every discrete point by means of the weighted linear sum associate with the function measures at all discrete locations selected regarding the solution field related to that spatial factor. Using a one-dimensional function, the HDQ and DQ calculations may be clearly exemplified. Based on the approaches, the estimated pth derivative connected to a function $f(x)$ is (Liew *et al.* 1999, Sobhani 2022a, b):

$$F(t)=(T*\eta)(t)=\int_{-\infty}^{+\infty}T(t-\xi)\eta(\xi)\,d\xi,\xi=r,\theta \quad (30)$$

Herein, $A_{ij}^{(1)}$ can be determined:

$$A_{ij}^{(1)}=\frac{\mathfrak{M}^{(1)}(x_i)}{(x_i-x_j)\mathfrak{M}^{(1)}(x_j)},i,j=1,2,\ldots,\mathfrak{N} \quad (31)$$

When $i=j$, the corresponding weighting coefficients are as follows:

$$\begin{aligned}A_{ii}^{(p)}=-\sum_{j=1,j\neq i}^{\mathfrak{N}}A_{ij}^{(p)},i=2,3,\ldots,\mathfrak{N}\ and\ p\\ =1,2,\ldots,\mathfrak{N}-1\end{aligned} \quad (32)$$

In Eq. (31), $\mathfrak{M}^{(1)}$ can be formulated by:

$$\mathfrak{M}^{(1)}(x_k)=-\sum_{j=1,j\neq k}^{\mathfrak{N}}(x_k-x_j),for\quad k= \quad (33)$$

$$1,2,3,\ldots,\mathfrak{N}.$$

3.2 Harmonic differential quadrature method (HDQM)

For $i \neq j$, the following formula yields the appropriate weights for the first-order derivatives $A_{ij}^{(1)}$ (Liew *et al.* 1999):

$$A_{ij}^{(1)} = \frac{\pi \mathfrak{P}(x_i)}{2\mathfrak{P}(x_j)\, sin[(x_i - x_j)/2\pi]}, i,j = 1,2,\ldots,\mathfrak{N}, \tag{34}$$

Herein,

$$\mathfrak{P}(x_i) = -\sum_{j=1,j\neq i}^{\mathfrak{N}} sin\left(\frac{\pi(x_i - x_j)}{2}\right), for\ j = 1,2,3,\ldots,\mathfrak{N}. \tag{35}$$

The 1st order derivatives $A_{ij}^{(1)}$ for $i = j$ have weights defined as:

$$A_{ii}^{(1)} = -\sum_{j=1,j\neq i}^{\mathfrak{N}} A_{ij}^{(1)}, for\ i = 1,2,3,\ldots,\mathfrak{N}. \tag{36}$$

Second-order derivative weights $A_{ij}^{(2)}$ for $i \neq j$ may be calculated by:

$$A_{ij}^{(2)} = A_{ij}^{(1)}\left(2A_{ij}^{(1)} - \pi ctg\left(\frac{x_i - x_j}{2} \times \pi\right)\right), i,j = 1,2,3,\ldots,\mathfrak{N} \tag{37}$$

For $i = j$, the derivatives $A_{ij}^{(2)}$'s weighting factors are as follows:

$$A_{ii}^{(2)} = -\sum_{j=1,j\neq i}^{\mathfrak{N}} A_{ij}^{(2)}, for\ \ i = 1,2,3,\ldots,\mathfrak{N}. \tag{38}$$

3.3 Two-dimensional approximation

From the one-dimensional situation, the HDQ and DQ approaches can be simply expanded to the three-dimensional approximation. The approximations regarding a two-dimensional unknown function $f\ (\mathbb{r},\theta)$ are given by the following formulas (Liew *et al.* 1999):

$$\left.\frac{\partial f}{\partial \mathbb{r}}\right|_{\mathbb{r}=\mathbb{r}_i,\theta=\theta_j} = \sum_{p=1}^{\mathfrak{N}_{\mathbb{r}}}\sum_{k=1}^{\mathfrak{N}_{\theta}} A_{ip}^{\mathbb{r}}\, I_{pk}^{\theta} f_{kj}, \tag{39a}$$

$$\left.\frac{\partial f}{\partial \theta}\right|_{\mathbb{r}=\mathbb{r}_i,\theta=\theta_j} = \sum_{p=1}^{\mathfrak{N}_{\mathbb{r}}}\sum_{k=1}^{\mathfrak{N}_{\theta}} I_{ip}^{\mathbb{r}}\, A_{pk}^{\theta} f_{kj}, \tag{39b}$$

$$\frac{\partial}{\partial \mathbb{r}}\left(\left.\frac{\partial f}{\partial \theta}\right|_{\mathbb{r}=\mathbb{r}_i,\theta=\theta_j}\right) = \sum_{p=1}^{\mathfrak{N}_{\mathbb{r}}}\sum_{k=1}^{\mathfrak{N}_{\theta}} A_{ip}^{\mathbb{r}}\, A_{pk}^{\theta} f_{kj}, \tag{39c}$$

$$\left.\frac{\partial^2 f}{\partial \mathbb{r}^2}\right|_{\mathbb{r}=\mathbb{r}_i,\theta=\theta_j} = \sum_{p=1}^{\mathfrak{N}_{\mathbb{r}}}\sum_{k=1}^{\mathfrak{N}_{\theta}} B_{ip}^{\mathbb{r}}\, I_{pk}^{\theta} f_{kj}, \tag{39d}$$

$$\left.\frac{\partial^2 f}{\partial \theta^2}\right|_{\mathbb{r}=\mathbb{r}_i,\theta=\theta_j} = \sum_{p=1}^{\mathfrak{N}_{\mathbb{r}}}\sum_{k=1}^{\mathfrak{N}_{\theta}} I_{ip}^{\mathbb{r}}\, B_{pk}^{\theta} f_{kj}. \tag{39e}$$

where $A_{ip}^{\mathbb{r}}$, A_{pk}^{θ}, $B_{ip}^{\mathbb{r}}$, and B_{pk}^{θ} indicate the weighing coefficients related to the *p*th partial derivatives associated with the function at the point (i, j) regarding the r and θ axes, and $\mathfrak{N}_{\mathbb{r}}$, and $\mathfrak{N}_{\theta}$ represent the total numbers related to discrete points selected throughout the r and θ directions. Also, the parameters $I_{ip}^{\mathbb{r}}$, I_{pk}^{θ}, $I_{ip}^{\mathbb{r}}$, and I_{pk}^{θ} indicate identity matrix.

Similarly, the Chebyshev–Gauss–Lobatto grid spreading can be supposed, regarding which the co-ordinates related to grid points $(\mathbb{r}_i, \theta_j)$ throughout the reference surface can be determined by (Tornabene 2009):

$$\mathbb{r}_i = \mathfrak{R}_i + \frac{\mathfrak{R}_o - \mathfrak{R}_i}{2}\left(1 - cos\left(\frac{(i-1)}{(\mathfrak{N}_{\mathbb{r}}-1)}\pi\right)\right) i = 1,2,3,\ldots,\mathfrak{N}_{\mathbb{r}}, \tag{40a}$$

$$\theta_j = \frac{\theta_m}{2}\left(1 - cos\left(\frac{(j-1)}{(\mathfrak{N}_{\theta}-1)}\pi\right)\right) j = 1,2,3,\ldots,\mathfrak{N}_{\theta}, \tag{40b}$$

Substitution of Eqs. (39a-e), and (27) into Eqs. (28a-e) and considering Eqs. (26a-i):

$$\left\{\begin{bmatrix}[\mathcal{F}_{dd}] & [\mathcal{F}_{db}]\\ [\mathcal{F}_{bd}] & [\mathcal{F}_{bb}]\end{bmatrix}\Delta\mathbb{T}_{c\mathbb{r}} + \begin{bmatrix}[\mathcal{K}_{dd}] & [\mathcal{K}_{db}]\\ [\mathcal{K}_{bd}] & [\mathcal{K}_{bb}]\end{bmatrix}\right\}\begin{Bmatrix}\Xi_d\\ \Xi_b\end{Bmatrix} = 0. \tag{41}$$

The thermal buckling related to the system are determined by Eq. (41). The BCs are organized by: The BCs are indicated by a four-letter phrase, where the 1st letter represents the BC at $= \mathfrak{R}_i$, the 2nd letter characterizes the BC at $\theta = 0$, the third letter denotes the BC at $\mathbb{r} = \mathfrak{R}_o$, and the fourth letter signifies the BC at $\theta = \theta_m$.

4. Introduction to deep neural networks for predicting engineering problems

Deep Neural Networks (DNNs) have emerged as a transformative tool in the field of engineering, providing powerful methodologies for modeling complex systems and predicting outcomes across various applications (Han *et al.* 2023). Leveraging multiple layers of interconnected nodes, DNNs excel at extracting intricate patterns from vast datasets, making them particularly suited for problems characterized by high dimensionality and non-linearity (Han *et al.* 2023). This paper explores the application of DNNs in predicting engineering problems, highlighting their architecture, advantages, and challenges (Taheri *et al.* 2021). DNNs are composed of an input layer, multiple hidden layers, and an output layer. Each layer consists of numerous neurons, each performing a weighted sum of inputs followed by a non-linear activation function (Liu *et al.* 2021). This hierarchical structure enables DNNs to learn increasingly abstract representations of data, facilitating the capture of complex relationships inherent in engineering problems (Taheri *et al.* 2020). Common architectures include feedforward networks, convolutional neural networks (CNNs), and recurrent neural networks (RNNs), each tailored to specific types of data and applications. DNNs have found diverse applications in various engineering disciplines. In structural engineering, for instance, DNNs are employed to predict the structural integrity of materials under various loads, assisting in the design of safer and more efficient structures. Similarly, in fluid dynamics, DNNs can model turbulent flow patterns, offering insights that traditional computational fluid dynamics methods may

Table 1 Correctness and convergence related to the thermal buckling parameter λ_T [$=12(1+\nu)\alpha\Delta T(a/h)^2$] belong to homogeneous circular plates with uniform temperature rise

$\frac{h}{R_o}$	Present	Ref. (Sepahi *et al.* 2011)	Ref. (Jalali *et al.* 2010)
Simply			
0.01	4.1990	4.2002	4.1973
0.02	4.1956	4.1964	–
0.05	4.1840	4.1853	4.1852
0.10	4.1465	4.1480	4.1480
0.15	4.0868	4.0875	–
0.20	4.0045	4.0056	4.0056
Clamped			
0.01	14.6881	14.6898	14.6758
0.02	14.6593	14.6609	–
0.05	14.5285	14.5301	14.5296
0.10	14.0889	14.0909	14.0909
0.15	13.4085	13.4157	–

Table 2 To search about a convergence study of the presented numerical solution procedure considering $h = 0.1\,nm,\ R_o = 40h,\ \theta_m = \frac{\pi}{4},\ n_{\mathbb{r}}, n_\theta, n_{\mathbb{Z}} = 1,\ l = h,\ \mu = h,$ $\emptyset_0 = 0.5$ (mV), $h_p = \frac{h}{10}$, and $A_p = \frac{A_{\mathbb{T}}}{2}$

Boundary conditions		$(\mathfrak{N}_{\mathbb{r}}, \mathfrak{N}_\theta)$					
		(5,5)	(7,7)	(9,9)	(11,11)	(13,13)	(15,15)
SSS	$K^p = 0$	249.3456	242.8954	242.6354	242.6354	242.6354	242.6354
	$K^p \neq 0$	272.6723	260.1265	260.0395	260.0395	260.0395	260.0395
CCC	$K^p = 0$	710.9843	698.4781	698.4412	698.4412	698.4412	698.4412
	$K^p \neq 0$	770.9843	751.8452	751.8081	751.8081	751.8081	751.8081

struggle to provide due to their computational intensity. In electrical engineering, DNNs are utilized in fault detection and diagnosis, where they analyze time-series data from sensors to identify potential anomalies in systems such as power grids or manufacturing equipment. In the realm of mechanical engineering, predictive maintenance can benefit from DNNs by forecasting equipment failures based on historical performance data, ultimately reducing downtime and maintenance costs. The primary advantage of DNNs lies in their ability to learn from large amounts of data without requiring explicit feature engineering. This is particularly beneficial in engineering applications where the relationships between input variables can be highly complex and not easily discernible. DNNs can also generalize well to unseen data, making them robust tools for predictive modeling. Moreover, DNNs can integrate heterogeneous data sources, such as numerical simulations, experimental data, and real-time sensor inputs, allowing for comprehensive analysis and enhanced predictive capabilities. Their scalability also means they can adapt to increasing data sizes and complexities, a critical factor in modern engineering challenges. Despite their advantages, DNNs present several challenges. The need for large labeled datasets for training can be a limiting factor, particularly in specialized engineering domains where data may be scarce. Additionally, DNNs can be prone to overfitting, requiring techniques such as regularization, dropout, or early stopping to ensure generalizability. Interpreting the decisions made by DNNs poses another challenge, as the "black box" nature of these models can hinder understanding and trust in their predictions. Future research may focus on developing more interpretable models or techniques that can elucidate the decision-making processes of DNNs. In summary, Deep Neural Networks represent a powerful paradigm for predicting engineering problems, offering advanced modeling capabilities that can drive innovation across various fields. As the availability of data continues to expand and computational resources become increasingly accessible, the integration of DNNs in engineering practice is likely to grow, paving the way for enhanced design, optimization, and operational strategies. Continued exploration of their limitations and potential improvements will be essential for maximizing their impact in engineering applications.

5. Results and discussion

Numerical scheming has been made regarding the sandwich circular NEMS composed of the PTZ-4 and FGM and composites with the material features given in Ref. (Reddy and Chin 1998, Pietrzakowski 2008).

5.1 Validation

To search about the accuracy of the current solution procedure, in Table 1 the thermal buckling of the homogeneous circular plates with uniform temperature rise of the current work is compared with the results of Refs. (Jalali *et al.* 2010, Sepahi *et al.* 2011). As is seen, the results are compared for different boundary conditions and $h/\mathfrak{R}_o$ parameters. As is presented, by increasing the $h/\mathfrak{R}_o$ parameter, the critical temperature of the homogeneous circular plates with uniform temperature rise decreases. Also, clamped supported boundary condition due to improved edge condition has higher critical temperature than simply supported boundary condition. From Table 3 can be seen that, there are good agreement between the results of current work and those of published articles in the literature.

5.2 Convergence study

To search about a convergence study of the presented numerical solution procedure, Table 2 is presented. According to this table, selecting nine grid points along with $\mathbb{r}$ and θ directions are appropriate for obtaining the exact result. Also, based on this figure, it can be concluded that clamped supported boundary condition due to improved edge condition has higher critical temperature than simply supported boundary condition.

5.3 Parametric results

The impacts of various parameters on the thermal

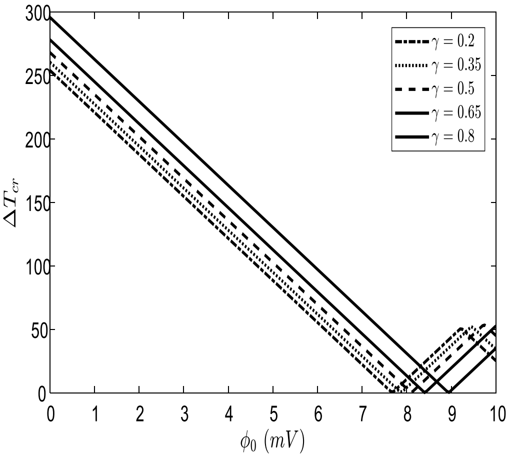

Fig. 2 The impacts of γ, and ϕ_0 parameters on the thermal buckling of the current sandwich circular NEMS considering $h = 0.1\,nm,\ R_o = 40h,\ \theta_m = \frac{\pi}{6},\ \mu = h,\ l = h$, $A_{\mathfrak{P}} = \frac{A_{\mathbb{T}}}{4}$, poroelastic system and CCC boundary conditions

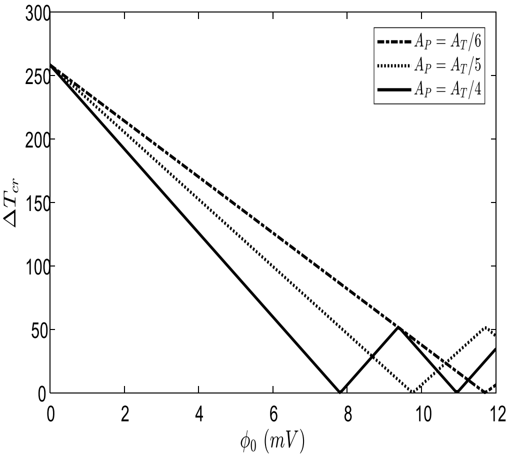

Fig. 3 The impacts of $A_{\mathfrak{P}}$, and ϕ_0 parameters on the thermal buckling of the current sandwich circular NEMS considering $h = 0.1\,nm,\ R_i = 40h,\ R_o = 2.5R_i,\ \theta_m = \frac{\pi}{6}$, $\mu = h,\ l = h$, and CCC boundary conditions

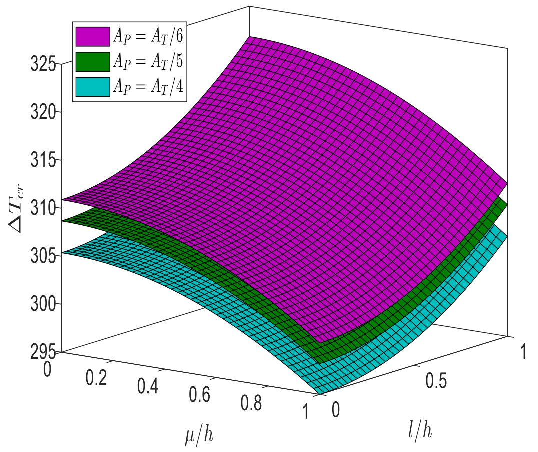

Fig. 4 The impacts of $A_{\mathfrak{P}}$, and nonlocal strain gradient parameters on the thermal buckling of the current sandwich circular NEMS considering $h = 0.1\,nm,\ R_o = 40h,\ \theta = \frac{\pi}{2},\ \emptyset_0 = 0.5\ (mV)$, and SSS boundary conditions

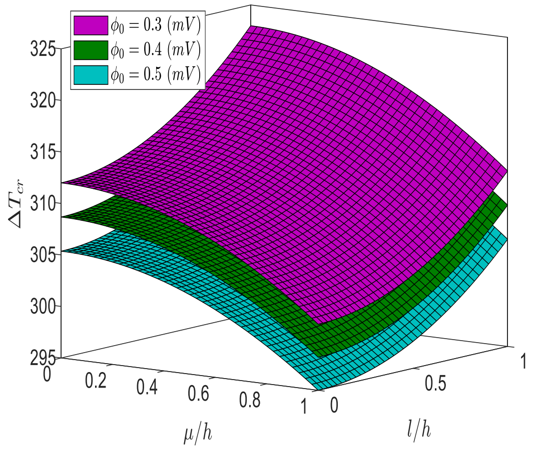

Fig. 5 The impacts of ϕ_0, and nonlocal strain gradient parameters on the thermal buckling of the current sandwich circular NEMS considering $h = 0.1\,nm,\ R_o = 40h,\ \theta = \frac{\pi}{2},\ A_{\mathfrak{P}} = \frac{A_{\mathbb{T}}}{4}$, and SSS boundary conditions

buckling of the current sandwich circular nanoplates are presented in this section. The impacts of γ, and ϕ_0 parameters on the thermal buckling of the current sandwich circular NEMS is shown in Fig. 2. According to Fig. 2, for greater γ values, ΔT_{cr} gets higher values and vice versa. Moreover, in an approximate range of 0 to 7.5, by increasing ϕ_0, ΔT_{cr} has a consistent decreasing trend, from then onwards, a raising trend with the same slope occurs which is followed by a decrease at the final range of ϕ_0.

The impacts of $A_{\mathfrak{P}}$, and ϕ_0 parameters on the thermal buckling of the current sandwich circular NEMS is presented in Fig. 3. As illustrated in Fig.3, although there is an equal amount for various $A_{\mathfrak{P}}$ amounts at ϕ_0=0, in an approximate ϕ_0 range of 0 to 8, the $A_{\mathfrak{P}}$ values equal to $A_T/4$ and $A_T/6$ has the least and the most ΔT_{cr} values, respectively. Moreover, by increasing ϕ_0, ΔT_{cr} has a reducing trend in which a fluctuation occurs in an approximate ϕ_0 range of 8 to 10 and therefore ΔT_{cr} values changes in a 0 to 50 range.

The impacts of $A_{\mathfrak{P}}$, and nonlocal strain gradient parameters on the thermal buckling of the current sandwich circular NEMS are shown in Fig. 4. Referring to Fig. 4, by reducing the *l*/*h*, values regarding ΔT_{cr} are descended. However, a rise in the μ/h causes a decreasing trend in ΔT_{cr}. The Ap values equal to $A_T/4$ and $A_T/6$ determine the minimum and maximum ΔT_{cr} amounts, respectively. It should be noted that for greater values of $A_{\mathfrak{P}}$, ΔT_{cr} also take fewer amounts, this fact is valid for variation regarding *l*/*h* and μ/h.

The impacts of ϕ_0, and nonlocal strain gradient parameters on the thermal buckling of the current sandwich circular NEMS are studied in Fig. 5. With regards to Fig. 5, fewer *l*/*h* values cause lower amounts of ΔT_{cr}. However, by

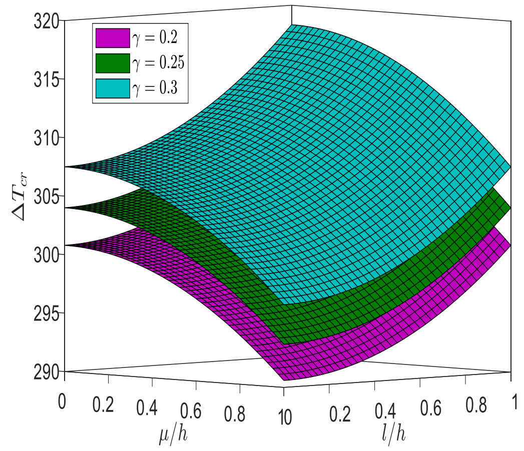

Fig. 6 The impacts of γ, and nonlocal strain gradient parameters on the thermal buckling of the current sandwich circular NEMS considering $h = 0.1\,nm$, $R_o = 40h$, $\theta = \frac{\pi}{2}$, $A_{\mathfrak{P}} = \frac{A_{\mathbb{T}}}{4}$, $\emptyset_0 = 0.5\ (mV)$, and SSS boundary conditions

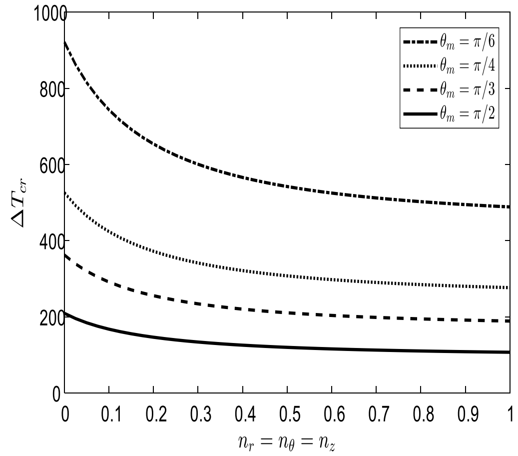

Fig. 7 The impacts of θ_m, and FG power index parameters on the thermal buckling of the current sandwich circular NEMS considering $h = 0.1\,nm$, $R_o = 40h$, $A_{\mathfrak{P}} = \frac{A_{\mathbb{T}}}{4}$, $\emptyset_0 = 0.5\ (mV)$, $\mu = h$, $l = h$, and SSS boundary conditions

raising μ/h, decreasing trend in ΔT_{cr} happens. The ϕ_0 values equal to 0.3 and 0.5 define the maximum and maximum ΔT_{cr} amounts, respectively. It should be noted that for greater values ϕ_0, ΔT_{cr} also takes fewer amounts, this fact is valid for variation regarding *l*/*h* and μ/h.

The impacts of γ, and nonlocal strain gradient parameters on the thermal buckling of the current sandwich circular nanopl NEMS ates are investigated in Fig. 6. As demonstrated in Fig. 6, higher *l*/*h* values cause greater amounts of ΔT_{cr}. However, by raising μ/h, values regarding ΔT_{cr} decreased. The γ values equal to 0.2 and 0.3 determine the minimum and maximum ΔT_{cr} values, respectively. In Addition, for greater values of γ, ΔT_{cr} also takes higher amounts, this fact is valid for variation regarding *l*/*h* and μ/h.

The impacts of θ_m, and FG power index parameters on the thermal buckling of the current sandwich circular NEMS are studied in Fig. 7. As Fig. 7 indicates, by

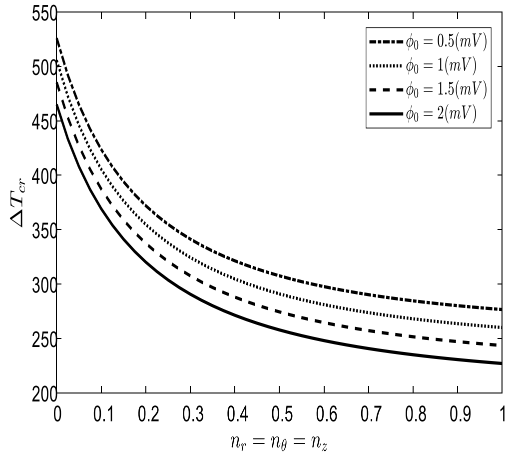

Fig. 8 The impacts of ϕ_0, and FG power index parameters on the thermal buckling of the current sandwich circular NEMS considering $h = 0.1\,nm$, $R_o = 40h$, $\theta_m = \frac{\pi}{4}$,, $A_{\mathfrak{P}} = \frac{A_{\mathbb{T}}}{4}$, $\mu = h$, $l = h$, and SSS boundary conditions

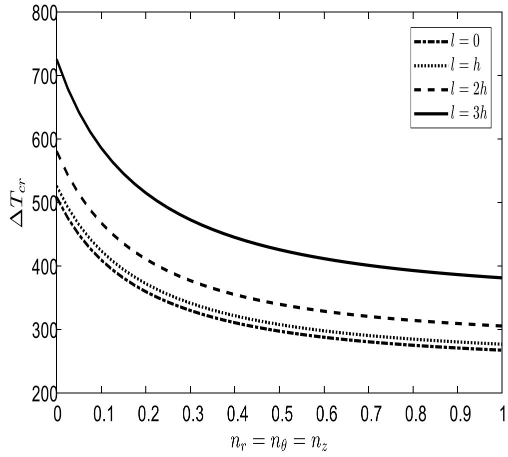

Fig. 9 The impacts of l, and FG power index parameters on the thermal buckling of the current sandwich circular NEMS considering $h = 0.1\,nm$, $R_o = 40h$, $\theta_m = \frac{\pi}{4}$,, $A_{\mathfrak{P}} = \frac{A_{\mathbb{T}}}{4}$, $\emptyset_0 = 0.5\ (mV)$, $\mu = h$, and SSS boundary conditions

increasing *n* values in the range of 0 to 1, values regarding ΔT_{cr} are decreased, which has a sharper trend in lower *n* values, while, negligible changes in ΔT_{cr} are observed for higher *n* values. It can be noticed that, the $\theta_m$values equal to $\frac{\pi}{2}$ and $\frac{\pi}{6}$ has the least and the most ΔT_{cr} values, respectively.

Fig. 8 presents the impacts of ϕ_0, and FG power index parameters on the thermal buckling of the current sandwich circular NEMS. As can be observed in Fig. 8, by increasing *n* values in the range of 0 to 1, values regarding ΔT_{cr} are reduced, which has a steeper trend for lower *n* values. It can be noticed that a greater value of ϕ_0, cause the ΔT_{cr} to take lower amounts. Generally, by increasing *n* values, ΔT_{cr} values related to different ϕ_0, get further apart.

The impacts of l, and FG power index parameters on the thermal buckling of the current sandwich circular

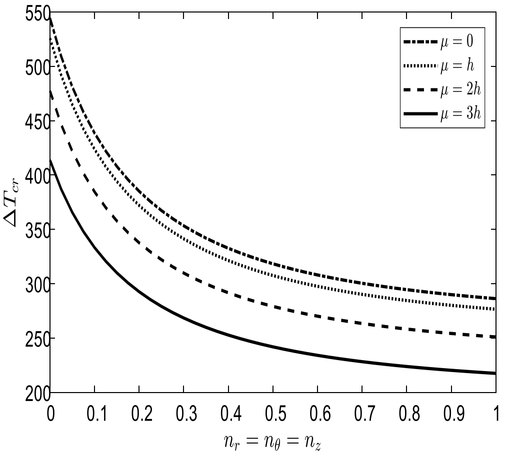

Fig. 10 The impacts of μ, and FG power index parameters on the thermal buckling of the current sandwich circular NEMS $h = 0.1\,nm,\ R_o = 40h,\ \theta_m = \frac{\pi}{4},\ A_{\mathfrak{P}} = \frac{A_{\mathbb{T}}}{4},\ \emptyset_0 = 0.5\ (mV),\ l = h$, and SSS boundary conditions

Table 3 investigating the G-DNNM hyperparameter parameter space and determining the ideal values for them

Hyperparameter	Box constraint	Kernel scale	Epsilon
Range	[0.01 -900]	[0.01-900]	[0.021-1450]
Optimum value	812.91	4.821	1.499

NEMS is shown in Fig. 9. From Fig. 9, it is clear that by increasing n, values regarding ΔT_{cr} are decreased, and the changes are negligible for higher n values. Moreover, l values equal to $3h$ and 0, allocate the most and the least values of ΔT_{cr}, respectively. This fact is valid for variation regarding n.

Fig. 10 shows the impacts of μ, and FG power index parameters on the thermal buckling of the current sandwich circular NEMS. In accordance with Fig. 10, by increasing n, values regarding ΔT_{cr} are decreased, and the changes are more noticeable for lower n amounts. It can be pointed out that, μ values equal to 3h and 0, get the least and the most values of ΔT_{cr}, respectively. This fact is valid for variation regarding n.

5.4 Deep neural networks prediction

Regression analysis is performed in the MATLAB environment using three machine learning techniques: Gaussian DNNM (G-DNNM), gradient boosting (LSBoost), and bootstrap aggregation (Bagging). Hyper-parameter optimization is carried by using the Bayesian optimization technique. Table 3 includes the hyperparameters and the corresponding search space for machine learning models. The Bayesian approach is used nine times to each machine learning model due to its probabilistic character. Using a 90-iteration threshold, we analyze 910 distinct hyper-parameter configurations for every model. Finally, we choose the option that would allow us to do regression analysis the best. The five-fold cross-validation procedure's mean squared error (MSE) is the objective function of Bayesian optimization. The order of the optimization process is shown in previous section, and the optimum solutions that were obtained are listed in Table 3. For the G-DNNM model, a kernel scale of 4.821, a box constraint of 812.91, and an epsilon value of 1.689 are the suggested values. A maximum of 26 splits, a learning rate of 0.158, a number of variables to sample of 2, a minimum leaf size of 3, and a learning cycle size of 352 are the hyperparameters that the LSBoost model performs best with. The following configuration is advised for the Bagging model: a minimum leaf size of 3, a maximum number of splits of 14, a learning cycle size of 369, and a number of variables to sample of 2.

6. Conclusions

NEMS-based sensors are used to detect thermal and mechanical stresses in aerospace structures. Knowledge of their thermal buckling properties ensures these sensors remain accurate and reliable under extreme thermal conditions, providing crucial data for structural health monitoring. To evaluate the electro-thermal buckling response of a 3D-PFG nanoplate patched with a piezo-electric layer in a thermal environment, this work detailed the creation of a 2D-HDQM combined with the RQ-3DTSDT. Couple equations using compatibility criteria were offered as a means of deriving the true governing equations. The nonlocal random sample generation technique NRLSGT was analyzed because it uses two variables, nonlocal and length scale factors, to model size effects. After obtaining the outputs of the mathematics, an appropriate dataset is used for testing, training and validating of the artificial intelligence. Numerical experimentation and comparison were used to prove the created method's correctness and efficacy. Following is a brief summary of the study's key findings:

- In a given ϕ_0, for greater γ values, ΔT_{cr} got higher values and vice versa.
- In an approximate ϕ_0 range of 0 to 8, the $A_{\mathfrak{P}}$ values equal to $A_T/4$ and $A_T/6$ had the least and the most ΔT_{cr} values, respectively.
- By reducing the l/h, values regarding ΔT_{cr} are descended. However, a rise in the μ/h caused a decreasing trend in ΔT_{cr}.
- For greater values of γ, ΔT_{cr} also took higher amounts, this fact is valid for variation regarding l/h and μ/h.
- By increasing n values, ΔT_{cr} values related to different applied voltage, got further apart.

This research explores the electro-thermal buckling behavior of 3D-PFG circular sector nanoplates patched with a piezoelectric layer, although it is important to note that these geometries are still very straightforward. High-complexity intelligent structures need to be researched to guarantee that the effort is worthwhile. The electro-pre buckling study solely considers the linear strain components of the structures. In contrast to huge amplitude, however, post-thermal buckling provides a more complete picture of the nanostructures' nonlinear static behavior. Future research into the electro-post thermal buckling response for very complex smart nanostructures is, thus, a promising area of inquiry.

Acknowledgment

The authors extend their appreciation to the Deanship of Research and Graduate Studies at King Khalid University for funding this work through Large Research Project under grant number RGP2/52/45.

Funding

This study was funded by Chongqing Technology Innovation and Application Development Plan Project (CSTB2024TIAD-CYKJCXX0033).

References

Alazwari, M.A., Zenkour, A.M. and Sobhy, M. (2022), "Hygrothermal buckling of smart graphene/piezoelectric nanocomposite circular plates on an elastic substrate via DQM", *Mathematics*, **10**(15), 10.3390/math10152638.

Alshenawy, R., Safaei, B., Sahmani, S., Elmoghazy, Y., Al-Alwan, A. and Nuwairan, M.A. (2022), "Buckling mode transition in nonlinear strain gradient-based stability behavior of axial-thermal-electrical loaded FG piezoelectric cylindrical panels at microscale", *Eng. Anal. Bound. Elem.*, **141**, 36-64, https://doi.org/10.1016/j.enganabound.2022.04.010.

Barretta, R., Feo, L., Luciano, R., de Sciarra, F.M. and Penna, R. (2016), "Functionally graded Timoshenko nanobeams: a novel nonlocal gradient formulation", *Compos. Part B Eng.*, **100**, 208-219. https://doi.org/10.1016/j.compositesb.2016.05.052.

Cao, J., Du, J., Fan, Q., Yang, J., Bao, C. and Liu, Y. (2024), "Reinforcement for earthquake-damaged glued-laminated timber knee-braced frames with self-tapping screws and CFRP fabric", *Eng. Struct.*, **306**, 117787. https://doi.org/10.1016/j.engstruct.2024.117787.

Chen, C., Yang, H., Song, K., Liang, D., Zhang, Y. and Ni, J. (2023), "Dissolution feature differences of carbonate rock within hydro-fluctuation belt located in the Three Gorges Reservoir Area", *Eng. Geol.*, **327**, 107362. https://doi.org/10.1016/j.enggeo.2023.107362.

Chen, N., Yan, P. and Ouyang, J. (2019), "A generalized approach on bending and stress analysis of beams with piezoelectric material bonded", *Sensor Actuat. A*, **290**, 54-61. https://doi.org/10.1016/j.sna.2019.02.029.

Drai, A., Daikh, A.A., Belarbi, M.O., Houari, M.S.A., Aour, B., Hamdi, A. and Eltaher, M.A. (2023), "Bending of axially functionally graded carbon nanotubes reinforced composite nanobeams", *Adv. Nano Res.*, **14**(3), 211-224. https://doi.org/10.12989/anr.2023.14.3.211.

Du, G., Zhang, H., Yu, H., Hou, P., He, J., Cao, S., Wang, G. and Ma, L. (2024), "Study on automatic tracking system of microwave deicing device for railway contact wire", *IEEE T. Instrum. Measur.*, **73**, 3527611. https://doi.org/10.1109/TIM.2024.3446638.

Eghbali, M. and Hosseini, S.A. (2024), "An accurate analytical exploration for dynamic response of thermo-electric CNTRC beams under driving harmonic and constant loads resting on Pasternak foundation", *Adv. Nano Res.*, **16**(6), 549-564. https://doi.org/10.12989/anr.2024.16.6.549.

Esen, I., Alazwari, M.A., Almitani, K.H., Eltaher, M.A. and Abdelrahman, A. (2023), "Dynamic vibration response of functionally graded porous nanoplates in thermal and magnetic fields under moving load", *Adv. Nano Res.*, **14**(5), 475. https://doi.org/10.12989/anr.2023.14.5.475.

Feng, Y., Mohammadi, M., Wang, L., Rashidi, M. and Mehrabi, P. (2021), "Application of artificial intelligence to evaluate the fresh properties of self-consolidating concrete", *Materials*, **14**(17), 4885. https://doi.org/10.3390/ma14174885.

Firouzianhaji, A., Usefi, N., Samali, B. and Mehrabi, P. (2021), "Shake table testing of standard cold-formed steel storage rack", *Appl. Sci.*, **11**(4), 1821. https://doi.org/10.3390/ma14174885.

Ghazwani, M.H., Alnujaie, A., Van Vinh, P. and Tounsi, A. (2024), "A quasi-3D nonlocal theory for free vibration analysis of functionally graded sandwich nanobeams on elastic foundations", *Adv. Nano Res.*, **16**(3), 313-324. https://doi.org/10.12989/anr.2024.16.3.313.

Gholami, R. and Ansari, R. (2017), "A unified nonlocal nonlinear higher-order shear deformable plate model for postbuckling analysis of piezoelectric-piezomagnetic rectangular nanoplates with various edge supports", *Compos. Struct.*, **166**, 202-218.

Han, S., Zheng, D., Mehdizadeh, B., Nasr, E.A., Khandaker, M.U., Salman, M. and Mehrabi, P. (2023), "Sustainable design of self-consolidating green concrete with partial replacements for cement through neural-network and fuzzy technique", *Sustainability*, **15**(6), 4752. https://doi.org/10.3390/su15064752.

Han, S., Zhu, Z., Mortazavi, M., El-Sherbeeny, A.M. and Mehrabi, P. (2023), "Analytical assessment of the structural behavior of a specific composite floor system at elevated temperatures using a newly developed hybrid intelligence method", *Buildings*, **13**(3), 799. https://doi.org/10.3390/buildings13030799.

Hu, D., Sun, H., Mehrabi, P., Ali, Y.A. and Al-Razgan, M. (2023), "Application of artificial intelligence technique in optimization and prediction of the stability of the walls against wind loads in building design", *Mech. Adv. Mater. Struct.*, 1-18. https://doi.org/10.1080/15376494.2023.2206208.

Huang, H., Yuan, Y., Zhang, W. and Li, M. (2021), "Seismic behavior of a replaceable artificial controllable plastic hinge for precast concrete beam-column joint", *Eng. Struct.*, **245**, 112848.

Huang, H., Li, M., Yuan, Y. and Bai, H. (2022a), "Theoretical analysis on the lateral drift of precast concrete frame with replaceable artificial controllable plastic hinges", *J. Build. Eng.*, **62**, 105386. https://doi.org/10.1016/j.jobe.2022.105386

Huang, H., Li, M., Zhang, W. and Yuan, Y. (2022b), "Seismic behavior of a friction-type artificial plastic hinge for the precast beam–column connection", *Arch. Civil Mech. Eng.*, **22**(4), 201. https://doi.org/10.1007/s43452-022-00526-1.

Huang, H., Li, M., Yuan, Y. and Bai, H. (2023), "Experimental research on the seismic performance of precast concrete frame with replaceable artificial controllable plastic hinges", *J. Struct. Eng.*, **149**(1), 04022222. https://doi.org/10.1061/JSENDH.STENG-1164.

Jalali, S., Naei, M. and Poorsolhjouy, A. (2010), "Thermal stability analysis of circular functionally graded sandwich plates of variable thickness using pseudo-spectral method", *Mater. Des.*, **31**(10), 4755-4763.

Jin, F., Qian, Z., Wang, Z. and Kishimoto, K. (2005), "Propagation behavior of Love waves in a piezoelectric layered structure with inhomogeneous initial stress", *Smart Mater. Struct.*, **14**(4), 515-523. https://doi.org/10.1088/0964-1726/14/4/009.

Ke, L.L. and Wang, Y.S. (2014), "Free vibration of size-dependent magneto-electro-elastic nanobeams based on the nonlocal theory", *Physica E*, **63**, 52-61. https://doi.org/10.1016/j.physe.2014.05.002

Khaje khabaz, M., Eftekhari, S.A., Hashemian, M. and Toghraie, D. (2020), "Optimal vibration control of multi-layer micro-beams actuated by piezoelectric layer based on modified couple stress and surface stress elasticity theories", *Physica A*, **546**, 123998. https://doi.org/10.1016/j.physa.2019.123998.

Kumar, P. and Harsha, S.P. (2020), "Modal analysis of functionally graded piezoelectric material plates", *Mater. Today Proc.*, **28**, 1481-1486. https://doi.org/10.1016/j.matpr.2020.04.825.

Kumar, P. and Harsha, S.P. (2022), "Static, buckling and vibration response analysis of three-layered functionally graded piezo-electric plate under thermo-electric mechanical environment", *J. Vib. Eng. Technol.*, **10**(4), 1561-1598. https://doi.org/110.1007/s42417-022-00467-2.

Li, J., Wang, Z., Zhang, S., Lin, Y., Jiang, L. and Tan, J. (2024), "Task incremental learning-driven Digital-Twin predictive modeling for customized metal forming product manufacturing process", *Robot. Comput. Integr. Manuf.*, **85**, 102647. https://doi.org/10.1016/j.rcim.2023.102647

Liew, K., Teo, T. and Han, J.B. (1999), "Comparative accuracy of DQ and HDQ methods for three-dimensional vibration analysis of rectangular plates", *Int. J. Numer. Meth. Eng.*, **45**(12), 1831-1848. https://doi.org/10.1002/(SICI)1097-0207(19990830)45:12<1831::AID-NME656>3.0.CO;2-W

Lim, C., Zhang, G. and Reddy, J. (2015), "A higher-order nonlocal elasticity and strain gradient theory and its applications in wave propagation", *J. Mech. Phys. Solid*, **78**, 298-313. https://doi.org/10.1016/j.jmps.2015.02.00

Liu, B., Yang, H. and Karekal, S. (2020), "Effect of water content on argillization of mudstone during the tunnelling process", *Rock Mech. Rock Eng.*, **53**, 799-813. https://doi.org/10.1007/s00603-019-01947-w.

Liu, J., Mohammadi, M., Zhan, Y., Zheng, P., Rashidi, M. and Mehrabi, P. (2021), "Utilizing artificial intelligence to predict the superplasticizer demand of self-consolidating concrete incorporating pumice, slag, and fly ash powders", *Materials*, **14**(22), 6792. https://doi.org/10.3390/ma14226792.

Liu, R., Li, H., Khadimallah, M.A. and Safarpour, M. (2022), "Three-dimensional poroelasticity solution of sandwich, cylindrical, open, functionally graded composite panels under multi-directional initial stress: semi-numerical modeling", *Arch. Civil Mech. Eng.*, **22**(1), 1-42. https://doi.org/10.1007/s43452-021-00337-w

Mallek, H., Jrad, H., Algahtani, A., Wali, M. and Dammak, F. (2019), "Geometrically non-linear analysis of FG-CNTRC shell structures with surface-bonded piezoelectric layers", *Comput. Meth. Appl. Mech. Eng.*, **347**, 679-699. https://doi.org/10.1016/j.cma.2019.01.001.

Mallek, H., Jrad, H., Wali, M. and Dammak, F. (2019), "Piezo-elastic response of smart functionally graded structure with integrated piezoelectric layers using discrete double directors shell element", *Compos. Struct.*, **210**, 354-366. https://doi.org/10.1016/j.compstruct.2018.11.062.

Mantari, J. and Soares, C.G. (2015), "A quasi-3D tangential shear deformation theory with four unknowns for functionally graded plates", *Acta Mechanica*, **226**(3), 625-642. https://doi.org/10.1007/s00707-014-1192-3.

Mehrabi, P., Honarbari, S., Rafiei, S., Jahandari, S. and Alizadeh Bidgoli, M. (2021), "Seismic response prediction of FRC rectangular columns using intelligent fuzzy-based hybrid metaheuristic techniques", *J. Ambient Intell. Human. Comput.*, **12**, 10105-10123. https://doi.org/10.3390/ma14174885.

Mehrabi, P., Shariati, M., Kabirifar, K., Jarrah, M., Rasekh, H., Trung, N.T., Shariati, A. and Jahandari, S. (2021), "Effect of pumice powder and nano-clay on the strength and permeability of fiber-reinforced pervious concrete incorporating recycled concrete aggregate", *Constr. Build. Mater.*, **287**, 122652. https://doi.org/10.3390/ma14174885.

Moradi-Dastjerdi, R. and Behdinan, K. (2021), "Free vibration response of smart sandwich plates with porous CNT-reinforced and piezoelectric layers", *Appl. Math. Modell.*, **96**, 66-79. https://doi.org/10.1016/j.apm.2021.03.013.

Moradi-Dastjerdi, R., Behdinan, K., Safaei, B. and Qin, Z. (2020), "Buckling behavior of porous CNT-reinforced plates integrated between active piezoelectric layers", *Eng. Struct.*, **222**, 111141. https://doi.org/10.1016/j.engstruct.2020.111141.

Pietrzakowski, M. (2008), "Piezoelectric control of composite plate vibration: Effect of electric potential distribution", *Comput. Struct.*, **86**(9), 948-954. https://doi.org/10.1016/j.compstruc.2007.04.023

Qiu, Y. (2019). "Estimation of tail risk measures in finance: Approaches to extreme value mixture modeling", Johns Hopkins University.

Qiu, Y. and Wang, J. (2024). "A Machine Learning Approach to Credit Card Customer Segmentation for Economic Stability", *Proceedings of the 4th International Conference on Economic Management and Big Data Applications*, ICEMBDA 2023, October, Tianjin, China.

Reddy, J. and Chin, C. (1998), "Thermomechanical analysis of functionally graded cylinders and plates", *J. Therm. Stress.*, **21**(6), 593-626. https://doi.org/10.1080/01495739808956165

Reddy, J.N. (2003), *Mechanics of Laminated Composite Plates and Shells: Theory and Analysis*, CRC press.

SafarPour, H., Ghanbari, B. and Ghadiri, M. (2019), "Buckling and free vibration analysis of high speed rotating carbon nanotube reinforced cylindrical piezoelectric shell", *Appl. Math. Modell.*, **65**, 428-442. https://doi.org/10.1016/j.apm.2018.08.028

Selim, B.A., Liu, Z. and Liew, K.M. (2019), "Active vibration control of functionally graded graphene nanoplatelets reinforced composite plates integrated with piezoelectric layers", *Thin Wall. Struct.*, **145**, 106372. https://doi.org/10.1016/j.tws.2019.106372.

Sepahi, O., Forouzan, M. and Malekzadeh, P. (2011), "Thermal buckling and postbuckling analysis of functionally graded annular plates with temperature-dependent material properties", *Mater. Des.*, **32**(7), 4030-4041. https://doi.org/10.1016/j.matdes.2011.03.063

Sharma, V. and Kumar, S. (2022), "Bleustein–Gulyaev wave in a nonlocal piezoelectric layered structure", *Mech. Adv. Mater. Struct.*, **29**(15), 2197-2207. https://doi.org/10.1080/15376494.2020.1854907.

Silva, T.M.P., Clementino, M.A., Erturk, A. and De Marqui, C. (2018), "Equivalent electrical circuit framework for nonlinear and high quality factor piezoelectric structures", *Mechatronics*. **54** 133-143. https://doi.org/10.1016/j.mechatronics.2018.07.009.

Sobhani, E. (2022a), "On the vibrational analysis of combined paraboloidal-conical air vehicle segment shell-type structures", *Aerosp. Sci. Technol.*, **129**, 107823. https://doi.org/10.1016/j.ast.2022.107823.

Sobhani, E. (2022b), "Vibrational performance modeling for coupling of a full-ellipsoid shell with a cylindrical shell with a focus on flexibility at coupling and boundary conditions via the GDQ-meshless method", *Eng. Anal. Bound. Elem.*, **144**, 329-351. https://doi.org/10.1016/j.enganabound.2022.08.037.

Sobhy, M., Abazid, M.A. and Al Mukahal, F.H.H. (2022), "Electro-thermal buckling of FG graphene platelets-strengthened piezoelectric beams under humid conditions", *Adv. Mech. Eng.*, **14**(4), 16878132221091005. https://doi.org/10.1177/16878132221091005.

Song, K., Yang, H., Liang, D., Chen, L. and Jaboyedoff, M. (2024), "Step-like displacement prediction and failure mechanism analysis of slow-moving reservoir landslide", *J. Hydrol.*, **628**, 130588. https://doi.org/10.1016/j.jhydrol.2023.130588.

Taheri, E., Firouzianhaji, A., Mehrabi, P., Vosough Hosseini, B. and Samali, B. (2020), "Experimental and numerical investigation of a method for strengthening cold-formed steel profiles in bending", *Appl. Sci.*, **10**(11), 3855. https://doi.org/10.3390/app10113855.

Taheri, E., Firouzianhaji, A., Usefi, N., Mehrabi, P., Ronagh, H. and Samali, B. (2019), "Investigation of a method for strengthening perforated cold-formed steel profiles under compression loads", *Appl. Sci.*, **9**(23), 5085. https://doi.org/10.3390/ma14174885.

Taheri, E., Mehrabi, P., Rafiei, S. and Samali, B. (2021), "Numerical evaluation of the upright columns with partial reinforcement along with the utilisation of neural networks with combining feature-selection method to predict the load and displacement", *Appl. Sci.*, **11**(22), 11056. https://doi.org/10.3390/app112211056.

Toghroli, A., Mehrabi, P., Shariati, M., Trung, N.T., Jahandari, S. and Rasekh, H. (2020), "Evaluating the use of recycled concrete aggregate and pozzolanic additives in fiber-reinforced pervious concrete with industrial and recycled fibers", *Constr. Build. Mater.*, **252**, 118997. https://doi.org/10.3390/ma14174885.

Tornabene, F. (2009), "Free vibration analysis of functionally graded conical, cylindrical shell and annular plate structures with a four-parameter power-law distribution", *Comput. Meth. Appl. Mech. Eng.*, **198**(37-40), 2911-2935. https://doi.org/10.1016/j.cma.2009.04.0

Wang, Z., Zhou, T., Zhang, S., Sun, C., Li, J. and Tan, J. (2023), "Bo-LSTM based cross-sectional profile sequence progressive prediction method for metal tube rotate draw bending", *Adv. Eng. Inform.*, **58**, 102152. https://doi.org/10.1016/j.aei.2023.102152.

Wu, J., Yang, Y., Mehrabi, P. and Nasr, E.A. (2023), "Efficient machine-learning algorithm applied to predict the transient shock reaction of the elastic structure partially rested on the viscoelastic substrate", *Mech. Adv. Mater. Struct.*, 1-25. https://doi.org/10.1080/15376494.2023.2183289.

Wu, Y., Fan, Y. and Li, L. (2022), "Nonlinear modal electro-mechanical coupling factor for piezoelectric structures containing nonlinearities", *Chinese J. Aeronaut.*, **36**(2), 100-110. https://doi.org/10.1016/j.cja.2022.06.020.

Xiao, C., Zhang, G., Yu, Y., Mo, Y. and Mohammadi, R. (2022), "Nonlinear vibration analysis of the nanobeams subjected to magneto-electro-thermal loading based on a novel HSDT", *Waves Random Complex Med.*, 1-20. https://doi.org/10.1080/17455030.2021.2023231.

Yaghoobi, H. and Torabi, M. (2013), "Post-buckling and nonlinear free vibration analysis of geometrically imperfect functionally graded beams resting on nonlinear elastic foundation", *Appl. Math. Modell.*, **37**(18-19), 8324-8340. https://doi.org/10.1016/j.apm.2013.03.037.

Yang, H., Chen, C., Ni, J. and Karekal, S. (2023), "A hyperspectral evaluation approach for quantifying salt-induced weathering of sandstone", *Sci. Total Environ.*, **885**, 163886. https://doi.org/10.1016/j.scitotenv.2023.163886.

Yang, H., Ni, J., Chen, C. and Chen, Y. (2023), "Weathering assessment approach for building sandstone using hyperspectral imaging technique", *Heritage Sci.*, **11**(1), 70. https://doi.org/10.1186/s40494-023-00914-7.

Yang, H., Song, K. and Zhou, J. (2022), "Automated recognition model of geomechanical information based on operational data of tunneling boring machines", *Rock Mech. Rock Eng.*, 1-18. https://doi.org/10.1007/s00603-021-02723-5.

Zhang, C., Hu, H., Ma, Q. and Wang, N. (2023), "Computational thermal stability and critical temperature buckling of nanosystem", *Adv. Nano Res.*, **14**(6), 575-590. https://doi.org/10.12989/anr.2023.14.6.575.

Zhang, C., Liu, Y., Zhang, Y., Ketabdar, A. and Xiang, H. (2024), "Study of educational management on performance of scholar in nano/micro-level composite", *Adv. Nano Res.*, **16**(6), 615-622. https://doi.org/10.12989/anr.2024.16.6.615.

Zhang, J., Li, Y. and Zhang, C. (2024), "Pounding induced overturning resistance of FPB-isolated structures considering soil-structure-interactions", *Soil Dyn. Earthq. Eng.*, **177**, 108416. https://doi.org/10.1016/j.soildyn.2023.108416

Zhang, J. and Zhang, C. (2023), "Using viscoelastic materials to mitigate earthquake-induced pounding between adjacent frames with unequal height considering soil-structure interactions", *Soil Dyn. Earthq. Eng.*, **172**, 107988. https://doi.org/10.1016/j.soildyn.2023.107988

Zhou, Y.T. and Luo, Q.H. (2022), "Asymmetric non-slipping adhesion behavior of layered piezoelectric structures", *Int. J. Mech. Sci.*, **224**, 107330. https://doi.org/10.1016/j.ijmecsci.2022.107330.

CC